229 (2023) 211937

Contents lists available at ScienceDirect

Geoenergy Science and Engineering

journal homepage: www.sciencedirect.com/journal/geoenergy-science-and-engineering

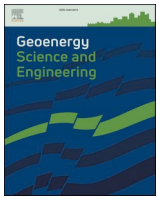

The pore-network modeling of gas-condensate flow: Elucidating the effect of pore morphology, wettability, interfacial tension, and flow rate

A. Hosseinzadegan [a], H. Mahdiyar [a], A. Raoof [b,*], E. Nikooee [c], J. Qajar [a]

[a] Department of Petroleum Engineering, School of Chemical and Petroleum Engineering, Shiraz University, Shiraz, Iran
[b] Department of Earth Sciences, Utrecht University, Utrecht, the Netherlands
[c] Department of Civil and Environmental Engineering, Shiraz University, Shiraz, Iran

ARTICLE INFO

Keywords:
Gas-condensate flow
Condensate blockage
Pore-network model
Snap-off
Wettability
Response surface methodology

ABSTRACT

The gas-condensate flow in the near-well region is significantly influenced by phase behavior, flow regimes, and pore geometries. In conventional gas-condensate reservoirs the key pore-scale parameters affecting gas and condensate relative permeabilities include velocity (i.e., pressure gradient), interfacial tension (IFT), wettability, and pore structure. To examine the impact of these parameters, three-dimensional (3D) and two-dimensional (2D) pore-network models (PNMs) were developed. A proposed compositional model was used to implement the cyclic process of condensate corner flow (film flow for circular tubes) and condensate blockage. Response surface methodology (RSM) was employed to achieve high accuracy in phase equilibrium calculations and to enhance computational speed.

The 3D PNM simulations of gas-condensate core-flood experiments confirmed the consistency and accuracy of the implemented methodology. A parametric study of governing factors such as pore shapes, wettability, IFT, and flow rate was conducted using the developed PNMs. The findings revealed that pore geometry and contact angle dictate the condensate meniscus curvature and snap-off process in pore throats. The unblocking of throats by condensate bridges was primarily controlled by contact angle, IFT, and pore cross-section. A shift to neutral wetting substantially improved gas-condensate flow in higher IFTs and angular pore shapes.

The positive velocity effect on low-IFT gas-condensate flow, known as the coupling rate effect, was more pronounced in simulations with lower contact angles, and its impact was negligible at neutral wettability, similar to the IFT effect. The simulation results and findings underscore the influence of each factor and offer a method for incorporating the effects of pore shape (i.e., formation type and structure), contact angle, velocity, and IFT in continuum scale simulations.

1. Introduction

Gas-condensate flow around the wellbore in conventional reservoirs is very different from the common immiscible incompressible two-phase oil and gas flow because of the complex velocity and IFT effects in this low-IFT flow system (i.e., coupling effect of viscous and capillary forces). The interplay of pore morphology, wettability and interfacial tension and their influence on porous medium permeability have not been studied in the context of gas-condensate flow, where the composition and mass transfer govern condensate phase creation and then mobilization and trapping of condensates is determined by the competition between viscous and capillary forces. The aforementioned competition and the influence of these factors on condensate mobilization is of course dependent on the velocity, wettability, pore shape and interfacial tension whereas condensate blockage is also influenced by the pore morphology, wettability and interfacial tension. The main differences between immiscible incompressible two-phase flow problems and gas-condensate flow involve the positive coupling effect as well as compositional variations due to mass transfer between phases during multicomponent transport in porous media below dew point pressure. Given the importance of the subject and the complexity of gas-condensate flow in porous media, there has been a wealth of studies on the gas-condensate flow and the physical factors controlling it. However, such studies, mostly core scale and experimental in nature, have rarely focused on the pore scale analysis of gas-condensate flow, and the effect of different pore morphologies. A pore-scale modeling approach,

* Corresponding author.
E-mail address: a.raoof@uu.nl (A. Raoof).

https://doi.org/10.1016/j.geoen.2023.211937
Received 20 January 2023; Received in revised form 16 May 2023; Accepted 21 May 2023
Available online 16 June 2023

accounting for the compositional changes has to be employed to investigate the intertangled effects of pore morphology, wettability and interfacial tension on the gas-condensate flow, and the pore scale mechanisms, which are macroscopically manifested in the gas-condensate relative permeability alterations under different reservoir conditions. This shortcoming has in fact been addressed in the current study.

Early experimental studies on the gas-condensate flow investigated the dependence of gas-condensate flow on IFT and condensate saturation (Bardon and Longeron, 1980; Asar and Handy, 1988; Haniff and Ali, 1990; Munkerud and Torsaeter, 1995) while later core-flood experimental studies revealed the positive velocity effect at low IFTs on the simultaneous flow of gas and condensate (Danesh et al., 1994; Henderson et al., 1995, 1996, 1997, 1998, 2001; Blom et al., 2000; Mott et al., 2000; Mahdiyar and Jamiolahmady, 2014; Gholampour and Mahdiyar, 2019). Those core-scale studies aimed at analyzing the effects of controlling parameters such as velocity and IFT on gas-condensate relative permeabilities, which are the backbone of flow simulators for predicting the well deliverability. For instance, Danesh et al. (1994) were the first ones to introduce the positive coupling rate effect, which is the positive effect of velocity on gas relative permeability. Some other studies focused on the direct experimental observation of the gas-condensate flow identifying the governing local rules with the aid of micromodels (Danesh et al., 1990; Coskuner, 1997; Jamiolahmady et al., 2000; Al-Kharusi, 2000; Al Harrasi, 2011; Al Harrasi et al., 2013). Using a high-pressure glass micromodel, Jamiolahmady et al. (2000) disclosed that the gas-condensate flow is governed by the cyclic process of gas-condensate flow in the throats (i.e., gas-flow path interruption by condensate blockage and gas flow re-establishment by gas pressure increase). Then, they developed a mechanistic model to implement the mentioned cyclic process. Their results confirmed the coupling rate effect on the gas-condensate relative permeability.

The studies of Jamiolahmady et al. (2000) highlighted the complex interactions among fluid flow, IFT and condensate formation and thus pointed out the need for pore-scale studies. In the subsequent years, the core flooding experiments reported a strong improvement effect of wettability change to the intermediate/gas-wetting conditions on gas-condensate flow. Those experiments mainly focused on the laboratory analysis of reservoir core samples by chemical treatment and confirmation of contact angle effect via spontaneous imbibition tests or core-flood experiments (Li et al., 2011; Zhang et al., 2014; Karandish et al., 2015; Al-Anazi et al., 2007; Liu et al., 2006; Noh and Firoozabadi, 2008; Fahimpour and Jamiolahmady, 2015; Hoseinpour et al., 2019).

Despite significant progress in the development of modeling approaches and simulation studies for gas-condensate flow (Panja et al., 2020), there is a pressing need for pore-scale models to more effectively assess the impact of various interacting parameters. Condensate formation is heavily influenced by the formation and movement of condensate bridges, which are governed by pore-scale mechanisms, such as snap-off. Consequently, the continued advancement of pore-scale models is a crucial aspect of gas-condensate flow research. Without this development, establishing reliable macroscopic constitutive relationships for gas-condensate systems, such as relative permeability, remains a challenging endeavor.

Pore-scale models can be categorized into two primary method groups. The first group employs a simplified representation of pore space, idealized as a collection of percolating or non-percolating geometric elements, such as pore-network models, capillary tube bundles, interacting capillary bundles, extended capillary tube bundles, pore morphology techniques, and pore unit assemblies (Raoof and Hassanizadeh, 2010; Khaksar et al., 2013, 2015; Nikooee et al., 2016; Sweijen et al., 2016, 2017; Daneshian et al., 2021; Cai et al., 2022; Hosseinkhani et al., 2023; Hosseinzadegan et al., 2023). The second group consists of direct numerical simulations (DNS) that involve detailed flow simulations performed directly on a comprehensive depiction of pore space (Raeini et al., 2015; Golparvar et al., 2018; Fathi et al., 2017; Zhao et al., 2019; Li et al., 2020; Mehmani et al., 2020; Cai et al., 2022). A thorough discussion on the advantages and disadvantages of pore-network modeling compared to other pore-scale models, such as phase-field, lattice Boltzmann (LB), smooth particle hydrodynamics (SPH), dissipative particle dynamics (DPD), volume of fluid (VOF), and level-set, is presented in Hosseinzadegan et al. (2023). Additionally, Yu et al. (2021) provide an extensive review of pore-scale models for modeling flow in unconventional reservoirs, with a specific focus on pore-network modeling and lattice Boltzmann.

While direct numerical simulations, such as lattice Boltzmann simulations, can offer detailed insights into processes like gas diffusion in the nanopore-scale structures of unconventional reservoirs (Yu et al., 2017, 2021), the simpler (coarser) porous structures of conventional gas-condensate reservoirs and the computational expense of direct numerical simulations make pore-scale models like pore networks an attractive alternative for modeling flow in conventional reservoirs. Pore-network modeling is based on a highly idealized depiction of porous media and significantly faster multiphase formulations, making it a suitable choice for exploring various scenarios required for stochastic modeling and parametric studies.

Pore-network model (PNM) simulation has been widely employed to investigate pore-scale phenomena in single or multiphase flow systems (Fatt, 1956; Koplik and Lasseter, 1985; Hui and Blunt, 2000; Blunt et al., 2002; Thompson, 2002; Al-Gharbi and Blunt, 2005; Piri and Blunt, 2005; Joekar-Niasar and Hassanizadeh, 2012; Raoof and Hassanizadeh, 2012). The PNM portrays the void space of a porous medium as a two or three-dimensional lattice consisting of pore bodies linked by pore channels (i.e., throats) (Raoof et al., 2013; Nikooee et al., 2014; Rostami et al., 2015; Daneshian et al., 2021). Pore-network models, much favored due to their lower computational cost are capable of capturing pore-scale physics (e.g., wettability and pore geometry and topology effects) and coupled processes in multiphase flow systems (Joekar-Niasar and Hassanizadeh, 2012; Xiong et al., 2016; Hosseinzadegan et al., 2023). In recent years, PNMs have, therefore, been employed to study the gas-condensate flow inspecting various pore scale phenomena of concern. Hosseinzadegan et al. (2023) present a comprehensive review of the pore-network models of gas-condensate flow. Hereafter, therefore, only a brief review of the major gas-condensate PNM studies is presented.

Mohammadi et al. (1990) developed a two-dimensional (2D) PNM and studied the effect of pore geometry and coordination number on the relative permeability in a capillary dominant flow regime using percolation theory. Fang et al. (1996) studied the IFT, pore shape, and contact angle hysteresis effect, and later on, Wang and Mohanty (1999) investigated the impact of pore and throat size, pore connectivity, and spatial correlation on critical condensate saturation through 2D PNMs considering both capillary and gravity effects. Then, Wang and Mohanty (2000) simulated the dynamic flow of gas and condensate in a cubic 3D PNM to study the impact of pore structure (i.e., geometry and aspect ratio) on relative permeability. Bustos and Toledo (2003, 2004) constructed 2D and 3D PNMs and analyzed the impact of pore size statistical properties, pore shape, and contact angle hysteresis on relative permeability, disregarding viscous forces. The effect of viscous forces was, however, taken into account by Li and Firoozabadi, 2000, who used a phenomenological condensation model and studied the impact of wettability alteration to intermediate-wet medium on critical condensate saturation and relative permeability in 2D networks. The interactions between gravitational, viscous and IFT on relative permeability were also studied. Jamiolahmady et al. (2003) and Momeni et al. (2017) investigated the coupling rate effect in a dynamic 3D bond PNM.

Momeni et al. (2017) pioneered the development of a dynamic semi-compositional two-phase flow model for gas-condensate systems, in which phase changes were accounted for using flash calculations at each time step, decoupled from the two-phase dynamic model. This approach aimed to improve quantification of condensate phase amounts

and properties within the flow model. Subsequently, two parallel studies on gas-condensate compositional pore-network modeling were conducted by Chen et al. (2020) and Santos and Carvalho (2020).

Chen et al. (2020) developed a 3D dynamic compositional pore-network model (PNM) for two-phase gas-condensate flow, examining the impact of phase changes on flow patterns within pore bodies under unsteady-state conditions. Their study introduced invasion by comparing capillary pressure and entry pressure, and primarily simulated a two-phase drainage process involving the injection of a gas mixture into a medium initially in the liquid state. They considered two different compositions and accounted for snap-off within pore throats. Their findings revealed that condensation of the injected gas phase and vaporization of the residual heavier component in the liquid phase significantly influenced gas fingering phenomena during unfavorable displacements at the pore scale.

Santos and Carvalho (2020) developed a 2D compositional PNM featuring straight cylindrical pore throats, designed for pore-scale simulation of retrograde condensation. They modeled gas-condensate molar flow under high capillary number flow conditions within the wellbore region, focusing on low interfacial tension and considering only film flow on the pore surfaces.

Utilizing the compositional model proposed by Santos and Carvalho (2020), which incorporates the snap-off effect, Reis and Carvalho (2020, 2021) investigated the influence of contact angle, velocity, and interfacial tension (IFT) on relative permeability curves within a 3D pore network consisting of pore elements exhibiting a converging-diverging profile. However, their research did not delve into the impact of varying pore geometries on the outcomes. In a separate study, Reis and Carvalho (2022) explored the mechanisms by which gas injection processes vaporize accumulated heavy components in the pore network, resulting from condensate blockage.

Advancements have been made not only in pore-network modeling of conventional gas-condensate reservoirs, which is the focus of the current study, but also in modeling unconventional reservoirs. In these reservoirs, the hydrocarbon mixture flow in the nanoporous structure of shale is significantly influenced by nanoscale flow physics and the heterogeneous pore structure (Yu et al., 2019; Song et al., 2020; Chen et al., 2021; Cui et al., 2022). Labed et al. (2018) developed a pore-network model (PNM) to characterize gas and condensate phase behavior in shales, analyzing flow patterns, pore size effects, and condensate blockage on Knudsen flow, while assuming minimal impact from capillary forces and gas adsorption-induced phase changes. Subsequently, Song et al. (2020) created a pore-network gas-condensate flow model based on a steady-state phase transport model and reconstructed 3D pore structure images. This model was used to study phase behavior and gas transport, taking into account pore shape, structure, interface curvature changes, gas slippage, and liquid phase boundary slip length in tight shale formations. The conventional thermodynamic model for phase equilibrium calculations was enhanced by considering the effects of oil-gas capillary pressure and spatial occurrence on fugacity balance. By incorporating the influence of capillary forces on phase saturation in nanoscale shale matrices, the researchers demonstrated that hydrocarbon mixture permeability is strongly affected by factors such as composition, pressure, temperature, multiscale heterogeneity, and wettability. For a more comprehensive review of PNM studies on unconventional reservoirs, readers are encouraged to consult Cui et al. (2022).

Gas-condensate flow in conventional reservoirs presents several unresolved questions that could be addressed through pore-network modeling, specifically utilizing the recently introduced dynamic compositional pore-network modeling (DCPNM). Gas-condensate flow in conventional reservoirs heavily relies on wettability. In particular, the intricate interplay of wettability, interfacial tension (IFT), flow rate, and pore geometry governs condensate trapping and mobilization, a crucial physical process that influences flow dynamics in gas-condensate systems. To the best of the authors' knowledge, this phenomenon has not been thoroughly analyzed using gas-condensate pore-scale models. Therefore, this study investigates the interaction and effects of pore geometry, IFT, flow rate, and wettability on the gas-condensate relative permeability in conventional reservoirs through a pore network approach. To achieve this, an efficient procedure for DCPNM of gas-condensate flow, considering the coupling between phase equilibrium and two-phase flow in conventional reservoirs, has been proposed. DCPNM was then employed to conduct an extensive parametric study elucidating the influences of these factors.

Existing procedures for dynamic compositional pore-network modeling typically utilize flash calculations for phase change calculations separately (Santos and Carvalho, 2020; Reis and Carvalho, 2021). However, only a few studies have considered modeling fluid flow in conjunction with phase equilibrium calculations, which can result in increased computational cost (Chen et al., 2020), rendering the model computationally expensive for an extensive parametric study. To address this, a response surface methodology was implemented, replacing the flash calculations in the proposed methodology. The obtained relative permeabilities in 3D models at steady-state conditions were compared to available experimental data and previous gas-condensate pore-network models (PNMs) in the literature, confirming the reasonable accuracy of the proposed methodology and the reliability of the mathematical formulations. Additionally, the positive velocity effect and the negative impact of IFT on gas-condensate relative permeabilities were examined, and the results are discussed.

The developed methodology is described in the following sections.

2. Pore-network models geometrical and topological description

In this study, a dynamic compositional pore-network model was mathematically formulated to consider the molar flow of gas and condensate in the network of pore throats and investigate the effects of major physical factors and pore morphology on the gas condensate flow in conventional porous media. We implemented condensation banking by the concept of snap-off and a cyclic process of condensate bridge formation and its displacement by the gas viscous force at different pressure gradients along the network.

Fig. 1 depicts this process in a representative pore element when the pressure level in the system is below the dew-point pressure (P_d). The pressure at outlet pore throats is set below the dew point, and inlet boundary conditions can be defined either as constant pressure or constant condensate-gas volume ratio (in this study the former has been used).

2.1. 3D model structure and morphology

A 3D model with triangular throats was constructed based on the statistical data derived from a Berea image (Dong, 2008), and the average coordination number was set to 3. The resulting 3D pore network was an equivalent spatial picture of the pore structure, and it was used to reproduce the experimental core flood data. For the pore throats, a prismatic shape and a triangular cross-sectional shape were selected based on the shape factors (i.e., the ratio of pore area to the square of its perimeter) obtained from a given pore shape distribution of a Berea core sample (Dong and Blunt, 2009; Yi et al., 2017) and depicted in Fig. 2(c). The mean of pore shape factors was 0.03, representing triangular throats, and the approach given by Patzek and Silin (2001) was implemented to calculate the angles of each throat cross-section. The inscribed radii of the pore throats were assigned based on a Weibull probability distribution function. Fig. 2(a–b) presents the pore size distributions and aspect ratios of a Berea digital core sample and those of our study. The pore throat radii were distributed between 1.28 μm and 19.21 μm, resulting in a mean value of 8.15 μm. The pore body radius was assigned according to the distribution of aspect ratio (i.e., the ratio of the pore body radius to the throat radius); $AR = R_b/R_b$ given for a Berea core sample. The distribution functions of the generated aspect

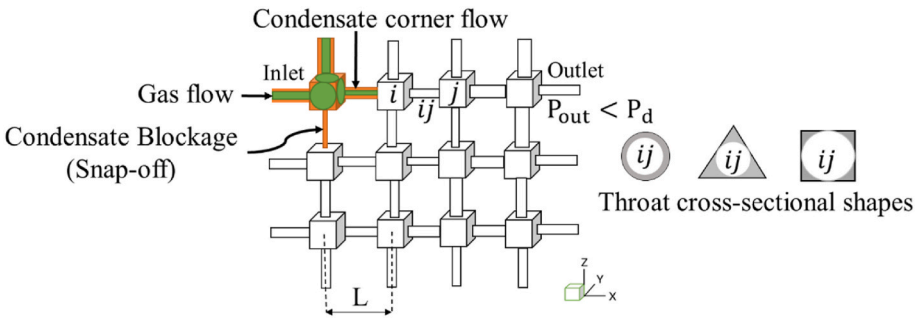

Fig. 1. The simplified two-dimensional pore network with different pore throat cross sectional shapes. A pore element is represented by pore body nodes *i* and *j* linked with a pore throat shown by *ij*-index.

ratio of our models and the distribution derived from a 3D image of a Berea sandstone given by Dong (2008) were depicted in Fig. 2(b). A representative cubic pore network of 20 × 20 × 20 nodes was used for PNM simulations neglecting the gravity effect. In addition, lattice lengths (the length between pore body centers) were set to a constant value of 90 μm to match the porosity (φ = 18.2%) and absolute permeability (K = 92mD) of the selected model to represent a Berea core sample used in core flood experiments by Jamiolahmady et al. (2003). As an exact match to the Berea core sample was not possible, a representative model with φ = 17.36% and K = 86 mD was considered close enough to the core sample.

2.2. 2D model

After validating the model and mathematical formulations, given the lower computational cost, 2D pore-network models with the dimensions of 25 × 25 × 1 were employed for the comprehensive parametric study to thoroughly investigate the effects of pore geometry, wettability, interfacial tension, and velocity on relative permeabilities using the proposed mathematical model. The effect of the selected dimension of the 2D network models was assessed before main parametric analysis simulations for a given condensate saturation and pore network statistical parameters (i.e., pore size distribution and aspect ratio) as well as pore geometry, at fixed wettability and flow conditions (i.e., the same IFT and velocity). After determining the minimum required network dimensions, three pore cross sections of the circle, square and equilateral triangle were selected, and the interplay effects of wettability and pore shape on the gas-condensate corner flow and snap-off in 2D simulations were examined.

Considering the reduced computational cost, 2D pore-network models were utilized for an extensive parametric analysis to thoroughly examine the impact of pore geometry, wettability, interfacial tension, and velocity on relative permeabilities. Consequently, 2D simulations aimed to quantify the effects of these contributing factors on process of gas-condensate blockage and mobilization, and in turn, the gas-condensate relative permeability. Although the simplistic 2D interconnectivity of the pore space may yield results that are not directly comparable to experiments conducted in actual reservoir rocks, the model can accurately represent most of the physical mechanisms associated with high capillary number flows of retrograde gas, which was the primary objective of this study. The 2D model effectively captures the interaction of pore morphology, interfacial tension, wettability, and velocity, whose influence on gas-condensate flow is of interest, and can thus be considered an alternative to (or a virtual counterpart of) microfluidic investigations of a gas-condensate system. However, the latter requires a sophisticated experimental setup to simulate reservoir temperature and pressure conditions. As a result, pore-network model studies, even those utilizing 2D models, can expedite the research process.

Similar to 3D simulations, the throat size and aspect ratio distributions for 2D models were generated based on Berea data, just like the 3D model. The receding contact angle was chosen to represent the displacement of the condensate by gas and to assess the influence of wettability changes on the resulting permeability curves, ranging from strongly liquid-wet conditions to neutral wetting at a 90-degree contact angle. It is important to note that a spatially uniform contact angle was employed in each simulation and varied for different cases, representing diverse wettability scenarios.

3. Mathematical model

The gas condensation process (the evolution of condensate blockage) around the production well, which varies as a function of time and phase behavior is a dynamic process due to compositional variation. To simulate the process of condensate trapping and mobilization, and its influence on gas condensate flow, a model accounting for the coupled multicomponent transport and dynamic two-phase flow governed by the competition of capillary and viscous forces is required. A dynamic compositional pore-scale model is therefore essential for accurately capturing this process. The mathematical framework of the developed component-based pore-network model is described considering the gas condensation at different pressure gradients.

In this study, flow properties were calculated using an equation of state (EOS), considering simultaneous gas and condensate flow in pore throats as a core-corner flow pattern before snap-off conditions. Pressure depletion-induced condensation led to condensate banking, increasing the number of closed throats. The model incorporated the cyclic process of throat opening and closing due to the interplay of capillary and viscous forces, using step functions described in the following section.

3.1. Gas-condensate flow process

Under wellbore flow conditions, the concurrent flow of gas and condensate is primarily influenced by capillary and viscous forces. Factors such as fluid flow properties, phase behavior, pore space geometry, and morphology also affect flow patterns in gas condensation systems. Pressure depletion results in more condensate dropouts, and an increase in the condensate radius of curvature in pore corners leads to gas blockage in restricted throats. This phenomenon, known as the snap-off process, causes the wetting phase liquid to form a bridge primarily located at throat mid-sections. Micromodel observations by Jamiolahmady et al. (2000) indicated that an increase in gas pressure can eliminate this condensate bridge due to viscous force. In other words, gas flow can be re-established, if the pressure drop along the throat surpasses a threshold capillary pressure value, termed entry pressure. Consequently, the gas-condensate flow functions as a cyclic process under the interaction of capillary and viscous forces, which is significantly influenced by pore geometry, contact angle, and fluid properties.

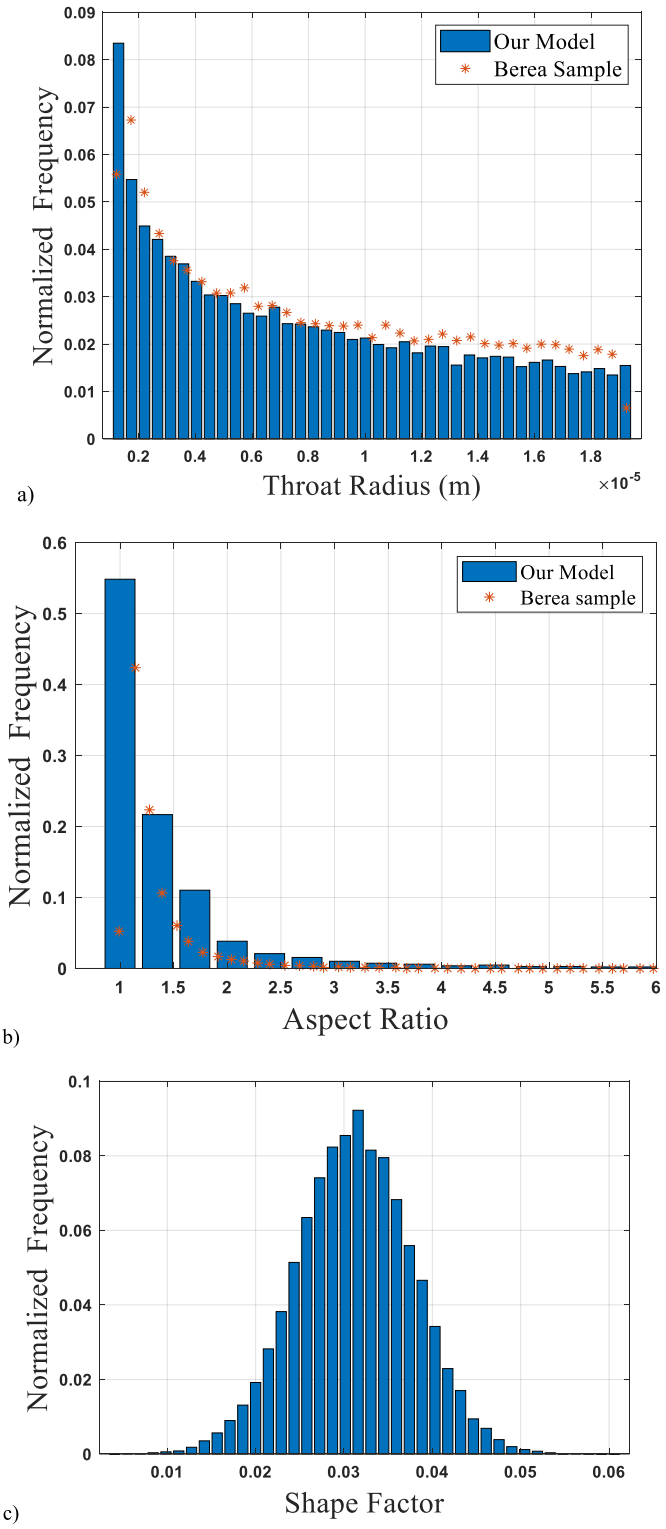

Fig. 2. 3D Model statistics: a) The throat-size distribution, b) The aspect ratio distribution compared with a 3D image of Berea sandstone given by Dong (2008), and c) The throat shape factor distribution adopted from a Berea sandstone (Dong and Blunt, 2009; Yi et al., 2017).

3.1.1. Fluid flow properties

The following flow properties and conditions were used to simulate flow conditions of core flooding experiments performed by Jamiolahmady et al. (2003) by means of the pore-network modeling approach. A binary mixture of methane and normal butane (C_1-nC_4) was introduced to the network, whose fluid initial conditions were set as presented in Table 1. Three pressure levels (1897 psi, 1853 psi, 1753 psi) and a temperature of 37 °C were considered to arrive at the experimental fluid properties (i.e., IFT and viscosity). The pressure levels correspond to the IFT values of 0.015, 0.04, and 0.15 mN/m. The first two IFT values are the same as those reported in the experimental data (Jamiolahmady et al., 2003) and the pressure of 1753 psi was considered to provide further insight into the effect of an increase in IFT due to a higher pressure decline in the reservoir. The modeling will be used to simulate gas-condensate flow at different flowing conditions for research purposes and provide variable flow paraments such as IFT and condensate dropout in the model.

Table 1
Selection of three pressure levels for gas condensation with corresponding IFT, gas and liquid viscosities at 37 °C.

Pressure (psi)	1897	1853	1753
IFT (mN/m)	0.015	0.04	0.15
μ_g (mPa.sec)	0.023	0.022	0.019
μ_l (mPa.sec)	0.036	0.038	0.043

3.1.2. Flow conditions for relative permeability calculation

In order to simulate the flow conditions in the pore network that correspond to the experimental conditions (i.e., to generate each point on the relative permeability curve), the molar composition of methane was chosen to attain the desired condensate saturation based on the phase diagram at the given experimental pressure level. Consequently, for the scenario with an inlet pressure of 1897 psi, the molar percentage of methane ranged from 80% to 75.5%; for the second case with an inlet pressure of 1853 psi, it ranged from 81.5% to 75%; and for the third case with an inlet pressure of 1753 psi, it ranged from 83% to 74.5%. These composition ranges established the initial conditions for the network, resulting in condensate dropouts (i.e., overall network condensate saturation) approximately between 1% and 30%, consistent with the experimental setup.

Subsequently, a range of pressure gradients was established along the network length for each case to achieve various flow velocities. The gas-condensate flow simulation proceeded until a steady-state flow was reached throughout the pore network (i.e., the average pressure within the entire network stabilized, and the molar flow between the inlet and outlet faces of the network converged). Ultimately, the flow rates of gas and condensate at the outlet face of the network were determined to generate relative permeability curves.

3.2. Assumptions

The water content was ignored for simplicity in the simulations. The gravity influence in all cases was neglected because the phase densities were close to each other at given fluid compositions, and pore throat lengths were relatively short (i.e., the gravity force acting by the condensate column was much lower than the magnitude of the viscous and capillary force in the vertical throats). Based on the review of Joekar-Niasar and Hassanizadeh (2012), it is computationally very expensive to track the interfaces within both pore throats and pore bodies, therefore in some pore-network models (see e.g., Aker et al., 1998; Knudsen and Hansen, 2002; Lovoll et al., 2005), it is assumed that the volume and resistance have been mainly assigned to throats, and the interface has not been tracked in pores, and no resistivity to flow has been assumed therein. Furthermore, in modeling gas-condensate flow in conventional reservoirs, for the reason that nanopores and pores of sizes comparable to throats are less abundant as compared to shales, commonly the bond model has been used and no interface in pores has been considered (please see for instance the works of Jamiolahmady et al. (2003) and Momeni et al. (2017), where the fluids were only distributed inside the pore throats meeting at nodes having no volume of

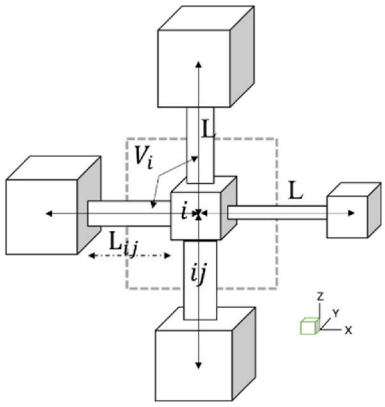

Fig. 3. Representation of a control volume V_i encompassing the volume of half throats entering that network node with i-index, connected to N_{cap} number of neighboring nodes with j-index. A throat is thus specified with the ij-index.

their own). Thus, all simulations were done via bond model, ignoring pore body nodes volumes and assuming that the pore body nodes have infinite conductivity because the gas-flow blockage is dominant in throats under the snap-off process.

Based on the previous observations in microfluidics (Jamiolahmady et al., 2000), the gas condensate flow patterns were modeled as a cyclic process consisting of condensate corner flow (film flow for circular throats), followed by condensate bridging in the throats due to snap off, and then condensate bridge displacement and redistribution in the adjacent throats under the effect of viscous forces. For all different fluid distributions in the model, constant pressure gradients (Dirichlet boundary conditions) were applied along the network to predict the relative permeabilities, following the same procedure used in previous studies (Wang and Mohanty, 2000; Santos and Carvalho, 2020; Song et al., 2020). The gas and liquid phases were supposed to be thermodynamically at equilibrium conditions instantly, and the porous matrix was also assumed to be incompressible with no chemical reactions. Considering angular pore shapes in conventional porous systems, the presence of condensate as a wetting film on the grain surfaces was ignored, as the condensate accumulated in the corners provides a much higher conductance as compared to the wetting film on the surface of the rock grains, in the angular pores, the similar assumption has been followed in the previous pore network studies (For angular shapes, please see quasi-static pore-network model of Bustos and Toledo (2003), dynamic pore-network model of Momeni et al. (2017)). This assumption may not be true in unconventional reservoir rocks such as shale matrix when the average pore radius is smaller than 100 nm and thereby the thin wetting film affects the fluid flow dynamics (i.e., connectivity and mobility) (He et al., 2021).

3.3. Governing equation

The molar conservation law presented in Eq. (1) was applied for all components in the defined control volume, V_i, which houses the pore body node and its connected half-length pore throats (shown as *ij*-index) to a pore body node, *i*, as depicted in Fig. 3. A control volume is placed at each node of the network, in which only the volumes of the throats ending at that node are considered.

$$-\sum_{j}^{N_{cap}} C_{ij}H_{ij}\left(T_{l_{ij}}+T_{g_{ij}}\right)\Delta\Phi_{ij}+Q_m=V_i\frac{\partial}{\partial t}\left(S_l x_m\overline{\rho}_l+S_g y_m\overline{\rho}_g\right)\ ;m=1\ldots n_c, \tag{1}$$

where $(T_{lij}+T_{gij})=(x_m\overline{\rho}_l g_l+y_m\overline{\rho}_g g_g)_{ij}$, Φ is the potential calculated in the throat, T is the transmissibility term, Q is the flow rate at the system's boundary, S is the saturation term, H is the step function, C is the pore-throat index, V is the control volume defined for each pore body node (with infinite conductivity), and N_{cap} is the number of throats connected to pore body, *i*. In addition, x_m and y_m are the mole fractions of component, m in the liquid and gas phase, $\overline{\rho}_l$ and $\overline{\rho}_g$ are the molar liquid and gas density, g_l and g_g refer to the liquid and gas conductance.

The derivation of the molar conservation equation is presented in Appendix A. The transmissibility of each phase flowing through the *ij*-index throats was defined as a function of the liquid and gas conductance (i.e., g_l, g_g), each component liquid and gas molar fractions (i.e., x_m, y_m), and molar densities (i.e., $\overline{\rho}_l$, $\overline{\rho}_g$). These terms were determined using the upwind approach (i.e., a throat property was interpolated on the upstream position of the two surrounding nodes) at the time counter (n+1) as follows:

$$T_{l_{ij}}^{n+1}=(x_m\overline{\rho}_l g_l)_{ij}^{n+1}=(x_m\overline{\rho}_l g_l)_i^{n+1}\quad ;if\ P_{g_i}>P_{g_j} \tag{2a}$$

$$T_{l_{ij}}^{n+1}=(x_m\overline{\rho}_l g_l)_{ij}^{n+1}=(x_m\ lg_l)_j^{n+1}\quad ;if\ P_{g_j}>P_{g_i} \tag{2b}$$

$$T_{g_{ij}}^{n+1}=\left(y_m\overline{\rho}_g g_g\right)_{ij}^{n+1}=\left(y_m\overline{\rho}_g g_g\right)_i^{n+1}\quad ;if\ P_{g_i}>P_{g_j} \tag{3a}$$

$$T_{g_{ij}}^{n+1}=\left(y_m\overline{\rho}_g g_g\right)_{ij}^{n+1}=\left(y_m\overline{\rho}_g g_g\right)_j^{n+1}\quad ;if\ P_{g_j}>P_{g_i} \tag{3b}$$

In conventional gas-condensate reservoirs, the capillary pressure effect on the phase equilibrium has been assumed negligible because of the coarser pore structure (Reis and Carvalho, 2021), and therefore, in Eq. (1) the potential term was formulated as presented in Eq. (4):

$$\Delta\Phi_{ij}=\Delta\Phi_{g,ij}=\Delta\Phi_{l,ij}=P_{g,i}-P_{g,j}-H_{ij}^{e}\Delta P_{ij}^{e} \tag{4}$$

where *ij* is the throat index connecting the pore body node, *i* to the pore body node, *j*. The term (ΔP_{ij}^{e}) was defined as throat entry pressure (P_{entry}) for the condensate bridge in the capillary, *ij*. The expressions (H_{ij}, H_{ij}^{e}) were defined as a function of throat entry pressure and critical gas saturation. In other words, H_{ij} and H_{ij}^{e} are unit step functions depending on gas saturation at the snap-off condition and entry capillary pressure for the condensate bridge in the throat, *ij*.

Critical gas saturation $(S_{g,crit})$ was defined as the gas saturation (S_g) at the critical condensate film thickness (t_{crit}) when the snap-off occurs. The pore-throat index (C_{ij}) was defined as zero if the pore throat is not connected to the pore body node, as (-1) if the pore throat enters the pore body node, and as $(+1)$ if the pore throat exits the pore body node.

In this proposed model, the volume consistency or saturation constraint (i.e., the summation of phase volumes equals to the control volume), which relates the pressure and molar phase properties in each control volume was fulfilled in the course of solving flow and phase-equilibrium equations (i.e., a set of equations is solved to calculate each phase property at equilibrium conditions). The phase viscosities, μ_g and μ_l, were obtained by applying the LBC correlation (Lohrenz et al., 1964). We assumed an isothermal flow of gas-condensate under thermodynamic equilibrium between gas and condensate in the pore bodies. The procedure for phase equilibrium calculations, known as flash calculations, is commonly implemented using an EOS (i.e., Peng and Robinson, 1976). For phase definition, as single phase or two-phase, the stability test given by Michelsen (1982) was implemented. The flash calculations were then required to be performed for the two-phase mixture at each time step to calculate all phase properties. During each time step, once the main variables were updated, a flash calculation can be performed for each control volume, V_i to determine new phase properties for the initial state of the next time step. More details for the procedure of phase equilibrium calculations using an EOS are given by Michelsen (1982), and Danesh (1998). It is noted that the phase equilibrium calculation has been coupled with gas-condensate pore-network models in pioneer studies by Jamiolahmady et al. (2003) and Chen et al. (2020). In this study, the flash calculations have been replaced with the

RSM as the RSM favors a less nonlinearity in the formulation, it has less computational time and, therefore, the equations derived from the RSM have been directly implemented in the calculations. During each simulation, phase properties required in flow terms calculations in the throats were assigned based on their upwind network node pressure and the overall composition.

3.4. Auxiliary equations

The position of phase interfaces at pore spaces is commonly governed by local rules governing the displacement of the main terminal and arc menisci in the pore bodies and pore corners. On this basis, the flow of gas and condensate phase in the present pore-network model was formulated based on entry pressure, the phase's hydraulic conductivity, and criteria for pore-scale processes (i.e., snap-off criterion), described hereafter in 3.4.1 and 3.4.2. The cyclic process of condensate bridging and displacement is also presented by the definition of step functions in section 3.4.3.

3.4.1. Entry capillary pressure and conductance

For single-phase laminar flow in a circular, triangular or square cross-section, the analytical expressions for conductance have been given by Oren et al. (1998) and Patzek and Silin (2001), applying Poiseuille's law. Multiphase flow through the pore corners in different geometries is more complex, and efforts have been directed to solve the fluid flow numerically using Navier-Stokes equations to derive conductivity terms for laminar corner flow correlated empirically with experimental works. In this study, we used the terms provided by Hui and Blunt (2000), which were successfully analyzed with laboratory results (Zhou et al., 1997; Firincioglu et al., 1999) and were applied in the mixed-wet random pore-scale network models. Piri and Blunt (2005) used these expressions and successfully simulated multiphase capillary-dependent physical processes at the pore scale. The conductance terms used in this study are presented in Table 2. The "free boundary condition" (i.e., the wetting boundary length at the liquid/gas interface is not supposed to generate flow resistance in the calculation of wetting conductance (Zhou et al., 1997)) suitable for gas-condensate interfaces was also considered. We assumed that the liquid phase wets the throats wall in a circular cross-section, and for square and triangle cross sections, the liquid phase flows as a corner flow, as shown in Table 2. The condensate conductivity is related to the resistance factor (β), contact angle, corner half angles, condensate corner area, viscosity, and interface radius of curvature. For entry pressures, the threshold capillary pressure of piston-like displacement in pore elements with non-circular cross-sections and different wettability is found using the MS-P theory (Mason and Morrow, 1991; Valvatne and Blunt, 2004). Entry pressures are derived from the conservation of energy applied to the main terminal meniscus (MTM) in a given pore by equating the virtual work of the MTM movement to the change in the surface free energy. Adopting the MS-P theory in the gas-condensate systems, once a condensate bridge was formed, the gas phase pressure difference exerted on the two sides of condensate is compared with the entry pressure of the throat defined in Table 2 for the throats of different cross sections.

Table 2
The entry pressure and related flow conductance terms for selected geometries.

Geometry: square cross section shown in Fig. 4	Refer Fig. 4
Entry pressure (Piri and Blunt, 2005)	When $\alpha < \frac{\pi}{2} - \theta_r$
	$P_{entry} = \frac{\sigma}{R}\left[cos\,\theta_r + \sqrt{\frac{tan\,\alpha}{2}(sin\,2\theta_r - 2\theta_r - 2\alpha + \pi)}\right]$ (5)
	where θ_r is the receding contact angle and α is the corresponding corner half angle
	when $\alpha \geq \frac{\pi}{2} - \theta_r$
	$P_{entry} = \frac{2\sigma}{R}(cos\,\theta_r)$ (6)
Flow conductance (Term g refers to flow conductance)	Non-wetting phase conductance: (Piri and Blunt, 2005; Chen et al., 2020)
	$g_{ij}^g = g_g = \frac{0.5623GA_g^2}{\mu_g l}$ (7)
	where G is the throat shape factor, A_g is area occupied by gas, μ_g is the gas viscosity and l is the length of capillary.
	Corner wetting-phase conductance for the corresponding corner half angle α when (Bustos and Toledo, 2003 adopted from Blunt, 1997; Hughes and Blunt, 2000):
	$when \;\; \alpha < \frac{\pi}{2} - \theta_r$
	$g_{ij}^l = g_l = \frac{V_l r_l^2}{\beta \mu_l l^2}$ (8)
	$V_l = n_c A_c l = n_c r_l^2 l\left[\sin(\alpha+\theta)\cos(\alpha+\theta) + \frac{cos^2(\alpha+\theta)}{\tan(\alpha)} - \frac{\pi}{2} + \alpha + \theta\right]$ (9)
	$A_c = A\left(1 - S_g\right) / n_c$ (10)
	where V_l refers to the condensate volume residing in the pore corners, n_c refers to the number of corners for a given polygonal cross-section and r_l refers to the meniscus radius of curvature defined in the pore corner as $r_l = \frac{\sigma}{P_c}$ in which σ, and P_c are the interfacial tension and the capillary pressure, respectively. Other parameters are the pore length, l, the pore corner half-angle, α, and the contact angle, θ.
	$\beta = \frac{12\,sin^2\,\alpha(1-C)^2(\psi_1 - C\psi_2)(\psi_3 + fC\psi_2)^2}{(1-sin\,\alpha)^2 C^2(\psi_1 - C\psi_2)^3}$ (11)
	$\psi_1 = cos^2(\alpha+\theta) + \cos(\alpha+\theta)\sin(\alpha+\theta)\tan(\alpha)$ (12)
	$C = \left(\frac{\pi}{2} - \alpha\right)\tan(\alpha)$ (13)
	$\psi_2 = 1 - \frac{\theta}{\frac{\pi}{2} - \alpha}$ (14)
	$\psi_3 = \frac{\cos(\alpha+\theta)}{cos\,\alpha}$ (15)

(continued on next page)

Table 2 (*continued*)

	Corner wetting-phase conductance for the corresponding corner half angle, α, is given by g_l in the following expression when: (Piri and Blunt, 2005) $\alpha \geq \frac{\pi}{2} - \theta_r$ $g_{ij}^l = g_l = \frac{A_c{}^2(1-sin\,\alpha)^2(\varphi_2\,cos\,\theta-\varphi_1)\varphi_3{}^2}{12\mu_l\,sin^2\,\alpha(1-\varphi_3{}^2)(\varphi_2+f\varphi_1)^2}$ (16) $\varphi_1 = \left(\frac{\pi}{2}-\alpha-\theta\right)$ (17) $\varphi_2 = \cot(\alpha)cos\,\theta - sin\,\theta$ (18) $\varphi_3 = \left(\frac{\pi}{2}-\alpha\right)\tan(\alpha)$ (19) $A_c = r_l{}^2\left(cos\,\theta(\cot(\alpha)cos\,\theta - sin\,\theta)+\theta+\alpha-\frac{\pi}{2}\right)$ (20) In the above formulation, $f = 0$ for the gas-condensate interface and the factor f varies between 0 and 1 according to the fluid interface boundary conditions.
Geometry: circular cross-section shown in Fig. 5	Refer Fig. 5
Entry pressure	The criterion for condensate bridge displacement: $P_{entry} = \frac{2\sigma}{R}(cos\,\theta_r)$ (21) where R is the radii of a capillary (Piri and Blunt, 2005)
Flow conductance (Term g refers to flow conductance)	$g_{ij}^g = g_g = \frac{0.5GA_g^2}{\mu_g l}$ (22) (Piri and Blunt, 2005) $g_{ij}^l = g_l = \frac{\pi\left(R^2 - S_g R^2\right)^2}{8\mu_l l}$ (23) where g and R are referred to as conductance and tube radius respectively. (Reis and Carvalho, 2021: in straight throats, the equivalent radius equals radius R)
Geometry: triangular cross-section shown in Fig. 6	Refer Fig. 6
Entry pressure	when $\alpha_1 < \frac{\pi}{2} - \theta_r$ $F_d = \frac{1+\sqrt{1-\frac{4GC}{cos^2\theta_r}}}{1+2\sqrt{\pi G}}$ (24) $P_{entry} = \frac{\sigma\,cos\,\theta_r}{r}\left(1+2\sqrt{\pi G}\right)F_d$ (25) $C = \sum_{i=1}^{n}\left[cos\,\theta_r\frac{\cos(\theta_r+\alpha_i)}{sin\,\alpha_i} - \left(\frac{\pi}{2}-\theta_r-\alpha_i\right)\right]$ (26) where α_1 is the sharpest corner half angle. G denotes the shape factor, θ_r stands for the receding contact angle, and α_i specifies the corresponding corner half angle (Piri and Blunt, 2005) $P_{entry} = \frac{2\sigma}{R}(cos\,\theta_r)$ (27) when $\alpha_1 \geq \frac{\pi}{2} - \theta_r$ (Piri and Blunt, 2005)
Flow conductance (Term g refers to flow conductance)	$g_{ij}^g = g_g = \frac{3GA_g{}^2}{5\mu_g l} = \frac{3R^2A_g}{20\mu_g l}$ (28) (Piri and Blunt, 2005) Corner wetting-phase conductance for the corresponding corner half angle α when: $\alpha < \frac{\pi}{2} - \theta_r$ $g_{ij}^l = g_l = \frac{A_c r_l^2}{\beta\mu_l l}$ (29) $A_c = r_l{}^2\left(cos\,\theta(\cot(\alpha)cos\,\theta - sin\,\theta)+\theta+\alpha-\frac{\pi}{2}\right)$ (30) $A_c = A\left(1-S_g\right)/n_c$ (31) β is the same factor as that defined for a square-shaped throat (Eq. (11)) Corner wetting-phase conductance for the corresponding corner half angle α when: $\alpha \geq \frac{\pi}{2} - \theta_r$ $g_{ij}^l = g_l$, the same expression as the one defined for a square-shaped throat (Eq. (16))

3.4.2. Snap-off criterion

In the context of gas-condensate PNMs, several snap-off criteria have been examined for capillary condensation. Threshold radius for throats, accounting for the condensate bridging formation in tight throats, have been considered by Mohammadi et al. (1990), Fang et al. (1996), and Wang and Mohanty (1999, Wang and Mohanty, 2000. On the other hand, Bustos and Toledo (2003) and Momeni et al. (2017) used the threshold capillary pressure, which corresponds to the condition where the gas phase will no longer have contact with the pore wall (i.e., at the snap-off pressure, an additional condensation process leads to the formation of condensate bridge). Jamiolahmady et al. (2003) employed a correlation that they derived from their mechanistic model (Jamiolahmady et al., 2000) developed in 2000, which determined the evolution time required for a condensate bridge to be created from an initial

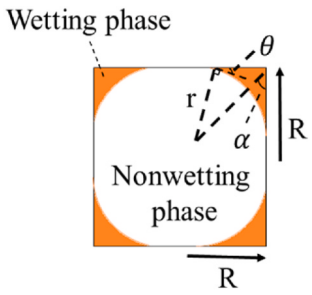

Fig. 4. Two-dimensional representation of the fluid configuration: a square cross-section capillary in the presence of two fluid phases. r refers to the radius of the fluid-fluid meniscus, R is the inscribed radius of the cross section, $\boldsymbol{\theta}$ stands for the contact angle of the wetting phase and α is the half-corner angle.

condensate thickness, depending on the throat shape, fluid properties, and initial condensate film thickness.

Reis and Carvalho (2020, 2021) identified a critical condensate film thickness for capillaries with a converging-diverging profile and circular cross-section. This thickness is proportional to the narrowing radius of each capillary, and they set the critical condensate film thickness to one-fourth of the narrowest radius, R_{min}. They also adopted the geometry-controlled condition given by Beresnev et al. (2009) for the fluid break-up in a sinusoidal-shaped pore-throat. In this study, for triangular and square cross sections, the criterion for the wetting phase curvature loss (with the throat wall) was considered in terms of a threshold capillary pressure. However, for circular cross sections, an assumed film thickness limit (critical film thickness equal to one-fourth of the throat radius) was used (see Table 3).

3.4.3. Step function definition

After snap-off, the displacement of condensate bridges in throats is controlled by the local entry capillary pressure, P_{entry}, which is presented in Table 2. The gas flow is re-established by the condensate bridge displacement when the gas pressure along each throat (i.e., ΔP_{ij}) exceeds the predefined entry pressure as a function of IFT between the phases, contact angle, pore geometry and pore radius. A step function is applied for the cyclic process of condensate blockage and displacement. In this approach, the conductance terms are multiplied by a continuous approximation of a unit step function, H_{ij} presented in Eq. (1). H_{ij} is set to unity when the condition for the throat corner flow (film flow for circular cross-sectional capillaries) of condensate is satisfied (i.e., the throat is open to annular gas and condensate corner flow), and set to zero when the gas flow is interrupted by the formation of a condensate bridge (and as long as the condensate bridge is not displaced). The term, H^e_{ij} is introduced for the condensate bridge displacement defined in Eq. (4), which is zero when we have the condensate corner flow (film) or the throat is blocked, and is one when the gas flow displaces the condensate bridge (in this case, H_{ij} is switched to one, please see flow chart presented in Fig. 7).

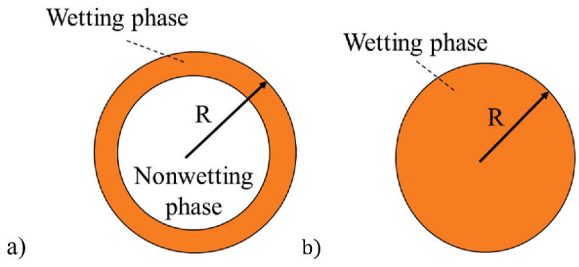

Fig. 5. The circular cross-section capillary in the presence of a) the wetting fim (condensate) flow on the surface of pore throat walls and b) the condensate bridge displacement under viscous displacement. *R* is the radius of circular pore throat.

3.5. Saturation distribution in the throats of a node

Jamiolahmady et al. (2003) initiated their pore-network model in dynamic mode with a fixed initial condensate saturation distributed in the network by filling the smallest pores. They assumed a thin film thickness for all remaining pores in their model. Under dynamic gas-condensate flow conditions, they determined the condensate film thickness from a proposed film thickness correlation in pores open to gas flow, which they had established earlier in a mechanistic study of condensate formation in a unit pore. Reis and Carvalho (2020, 2021) implemented the gas-condensate annular flow by a condensate thickness related to condensate saturation calculated from the compositional pore-network model in wide-open capillaries. When a throat was in a closed state, they considered a condensate bridge housed at the narrowest position in the throat within its maximum capillary pressure difference. In the current work, the condensate saturation in connecting throats is determined by distributing the total liquid molar volume in a control volume to its connecting throats (i.e., considering half of each throat attributed to a control volume and with respect to its molar volume). This approach leads to the formation of condensate bridges in tiny throats first and then in larger size throats, as reported in previous studies (Jamiolahmady et al., 2003). Moreover, if the gas phase can mobilize condensate bridges, the condensate would flow into the corresponding control volume at the considered node, then based on the molar balance of the wetting phase at that control volume, the saturation of the throats residing therein would be updated. Fig. 8 shows the implementation of this approach in a pore body node with control volume, V_i, with N_{cap} number of connecting pore throats with index, *ij* to a pore body node with index, *i*. In this approach, the total liquid molar numbers in each pore body control volume V_i, is determined as a function of the control volume, V_i, molar liquid density, $\overline{\rho}_{Li}$, and liquid saturation, S_{li}. Considering the control volume composed of N_{cap} capillaries (N_{cap} denotes the number of the throats, half of whose lengths is inside the control volume), N_{Li} as the total moles of liquid in the control volume, $V_{ij/2}$ as the volume of the half-length throat, and $\overline{\rho}_{lij/2}$ as the liquid molar density, each half-length throat liquid saturation $S_{lij/2}$, can be approximated by Eq. (32d). In this method, densities in the throats are evaluated according to the upstream gas pressure. This approach is consistent with core flood experiments presented in retrograde condensation because it gives thin condensate thickness for large-size throats and larger condensate thickness up to pore throats' radii for smaller throats in the whole pore network.

$$N_{Li} = V_i \overline{\rho}_{li} S_{li} \tag{32a}$$

$$N_{L\frac{ij}{2}} = V_{\frac{ij}{2}} \overline{\rho}_{l\frac{ij}{2}} S_{l\frac{ij}{2}} \tag{32b}$$

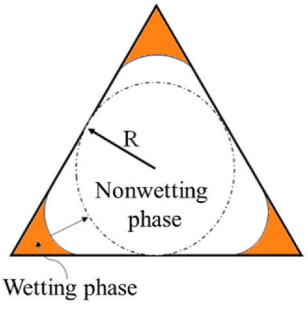

Fig. 6. Two-dimensional representation of the fluid configuration in a triangular cross-section capillary presenting the wetting phase (condensate) corner flow and the non-wetting phase flow in the center. R is the inscribed radius of the cross section.

Table 3
The snap-off criterion for selected geometries.

Geometry	Snap-off pressure, P_s	Critical gas saturation, $S_{g,\,crit}$ at snap-off condition
Square cross section (Bustos and Toledo, 2003)	$P_s = \frac{\sigma\cos(\alpha+\theta)}{R_t\cos\alpha}$ where R_t is the throat inscribed radius.	≈78.5%
Equilateral triangle cross section (Piri and Blunt, 2005)	For $\theta \le \frac{\pi}{2} - \alpha$ $P_s = \frac{\sigma}{R_t}(\cot\alpha\cos\theta - \sin\theta)$	≈60%
Circular cross section (Reis and Carvalho, 2021)	$R_c = 0.25\ R_t$ where R_c is the condensate thickness	≈56.25%

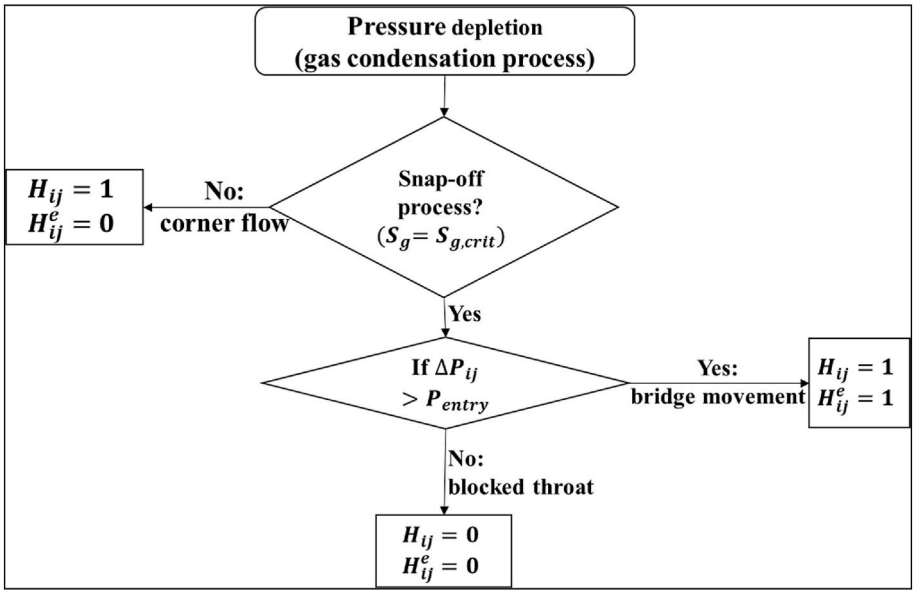

Fig. 7. Definition of the cyclic process of condensate blockage and displacement by step functions in the mathematical model.

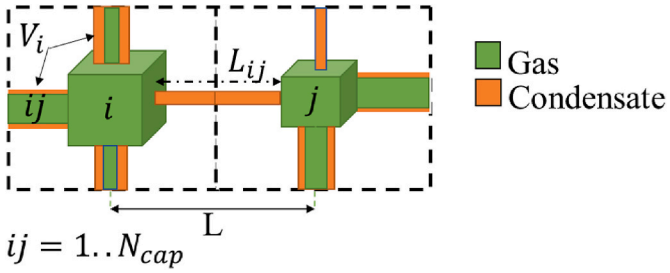

Fig. 8. The definition of a pore volume and the evolution of condensate phase in the connecting throats.

$$N_{Li} = V_i\overline{\rho}_{li}S_{li} = \sum_{j=1}^{N_{cap}} V_{ij}\overline{\rho}_{l\frac{ij}{2}}S_{l\frac{ij}{2}} \tag{32c}$$

$$S_{l\frac{ij}{2}} \approx (V_i\overline{\rho}_{li}S_{li}) \Big/ \left(\sum_{j=1}^{N_{cap}} V_{\frac{ij}{2}}\overline{\rho}_{l\frac{ij}{2}}\right) \approx (N_{Li}/N_{cap}) \Big/ \left(V_{\frac{ij}{2}}\overline{\rho}_{l\frac{ij}{2}}\right) \tag{32d}$$

3.6. Initial/boundary conditions

The absolute permeability is calculated by setting the initial pressure and composition of the network above the dew point pressure (i.e., to achieve a single-phase gas flow). Then the pressure at the outlet face of the network is set to a lower value applying a small pressure gradient across the network while keeping the inlet at the defined initial pressure condition.

To calculate each point of the relative permeability curve, the initial state of the system is defined in order to represent a two-phase gas-condensate flow. The initial gas-condensate flow at time = 0 is defined with an initial pressure as $P_{0i} = P_{inlet} = P_i$, an initial mixture composition as $Z_{0i} = Z_i$ (i stands for each pore body control volume), and an outlet boundary pressure denoted as $P_{outlet} = P_i - \Delta P$, where ΔP is a small pressure gradient defined based on the system flow rate, and Z_i is the considered compositions discussed in section 3.1.2. P_{inlet} and P_{outlet} are the pressures fixed at the inlet and outlet face of the pore network respectively (see Fig. 1).

Table 4
List of unknowns and equations in the compositional model formulation.

Unknowns:		Equations:		
Fluid Pressures	P_l , P_g	1	Overall composition constraint (Eq. (33))	1 equation
Fluid Saturations	S_l , S_g	2	Condensate equilibrium equations (Eq. (34))	n_c-equations
Overall Composition	$Z_m, m = 1...n_c$	3	Gas equilibrium equations (Eq. (35))	n_c-equations
Condensate Composition	$x_m, m = 1...n_c$	4	Vapor fraction/saturation relationship (Eq. (36a))	1 equation
Gas Composition	$y_m, m = 1...n_c$	5	Saturation constraint (Eq. (37))	1 equation
Total	$3n_c + 4$ unknowns	6	Capillary pressure relationship (Eq. (38))	1 equation
		7	Differential molar balances (Eq. (39))	n_c-equations

Table 5
List of main and supplementary equations in the compositional model formulation.

1	$\sum_{m=1}^{n_c} Z_m = 1$	(33)
2	$x_m = \frac{Z_m}{1 + n_V(K_i - 1)} \quad ; m = 1 \ldots n_c$ where $K_i = y_m / x_m$.	(34)
3	$y_m = \frac{K_i Z_m}{1 + n_V(K_i - 1)} = K_i x_m \quad ; m = 1 \ldots n_c$	(35)
4	$S_g = \frac{n_V \overline{\rho}_l}{\left((1 - n_V)\overline{\rho}_g + n_V \overline{\rho}_l\right)}$	(36a)
	$f_{gm} = f_{lm} \quad ; m = 1 \ldots n_c$	(36 b)
	where f_{gm} is the fugacity term for the m_{th} component in gas phase and f_{lm} is the fugacity term for the m_{th} component in liquid phase.	
5	$S_g + S_l = 1$	(37)
6	$P_l = P_g - P_c$ Assuming $P_c = 0$ in the pore body nodes: $P_l = P_g$.	(38)
7	$-\sum_{j}^{N_{cap}} C_{ij} H_{ij} \left[\left(x_m \overline{\rho}_l g_l + y_m \overline{\rho}_g g_g \right)_{ij} \right] \Delta \Phi_{ij} + Q_m = V_i \frac{\partial}{\partial t} \left(S_l x_m \overline{\rho}_l + S_g y_m \overline{\rho}_g \right), m = 1 \ldots n_c$ With the assumption of zero capillary pressure the potential gradient is defined as: $\Delta \Phi_{ij} = \Delta \Phi_{g,ij} = \Delta \Phi_{l,ij}$.	(39)

3.7. Compositional model formulation

The compositional model equations are represented with ($3n_c$+4) unknowns, which involves ($3n_c$+4) equations as shown in Table 4 (n_c stands for number of components). In this work, the number of components is two; hence, the model has ten unknowns requiring ten equations to be solved. The list of supplementary equations together with the main conservation equation is presented in Table 5.

To simplify the system of equations, the number of unknowns is reduced, and the eliminated variables are calculated after determining primary unknowns based on the supplementary equations. For this purpose, the gas pressure and the overall composition are selected as the primary variables defined in each control volume; the gas and condensate saturations are calculated during each flash calculation, which was replaced by RSM as linear functions in the simulations considering an incompressible porous medium due to tiny pressure change at the micro scale. In the procedure of phase equilibrium calculations at a given mixture composition, Z_m, pressure, P and temperature, T, the constraint equation given in Eq. (33) is always fulfilled. In addition, the total molar vapor and liquid fraction (n_V and n_L), the n_c-components fraction in the liquid and gas phase (x_m and y_m) are calculated at the thermodynamic equilibrium condition (Eq. (36b)) using an equation of state.

With the assumption of zero capillary pressure in the pore body nodes, the gas and condensate phase pressures are considered equal. As a result, the system of the molar conservation equations is solved for the gas phase pressure. The main set of governing differential equations (Eq. (39)) is coupled with the phase equilibrium calculations (provided above) as well as the saturation constraint equation (Eq. (37)). Finally, the solution technique, which is described in the next section is implemented to determine the variables.

3.8. Solution technique, model algorithm

The system of nonlinear equations is derived from molar conservation written for all pore body nodes, discretized, and expressed in the form of residual functions. A Newton-Raphson method was applied to solve for the primary unknown variables. Based on this approach, all residual functions are linearized, and all principal variables are calculated and updated using an iterative scheme to find the solution to these main variables at each time step. The procedure for time step selection is presented in Appendix B.

Defining X as the vector of primary variables, R as the residual functions, τ as the iteration number, and n as the time step counter, the linearization approach for each pore body node, i leads to:

$$\left[J^{n+1}\right]^{\tau} . \left[\Delta\delta^{n+1}\right]^{\tau+1} = \left[-R^{n+1}\right]^{\tau} \tag{40a}$$

where J is the Jacobian matrix containing numerical derivatives of residual functions concerning principal variables, and $\Delta\delta$ is the difference between primary variables during each iteration, as follows:

$$(X)^{\tau+1} - (X)^{\tau} = \left[\Delta\delta^{n+1}\right]^{\tau+1} \tag{40b}$$

$$(X)^{\tau+1} = (X)^{\tau} - \left(J^{-1}R\right)^{\tau} \tag{40c}$$

$$J = \frac{\partial R}{\partial X} \tag{40d}$$

Having defined the tolerance value, if the system of equations converged to the desired solution with an acceptable error, the solution is set to the new unknowns and the simulation moves on to the next time step. The solution of the principal variables could be achieved when $R \rightarrow 0$ that is $(X)^{\tau+1} \rightarrow (X)^{n+1}$.

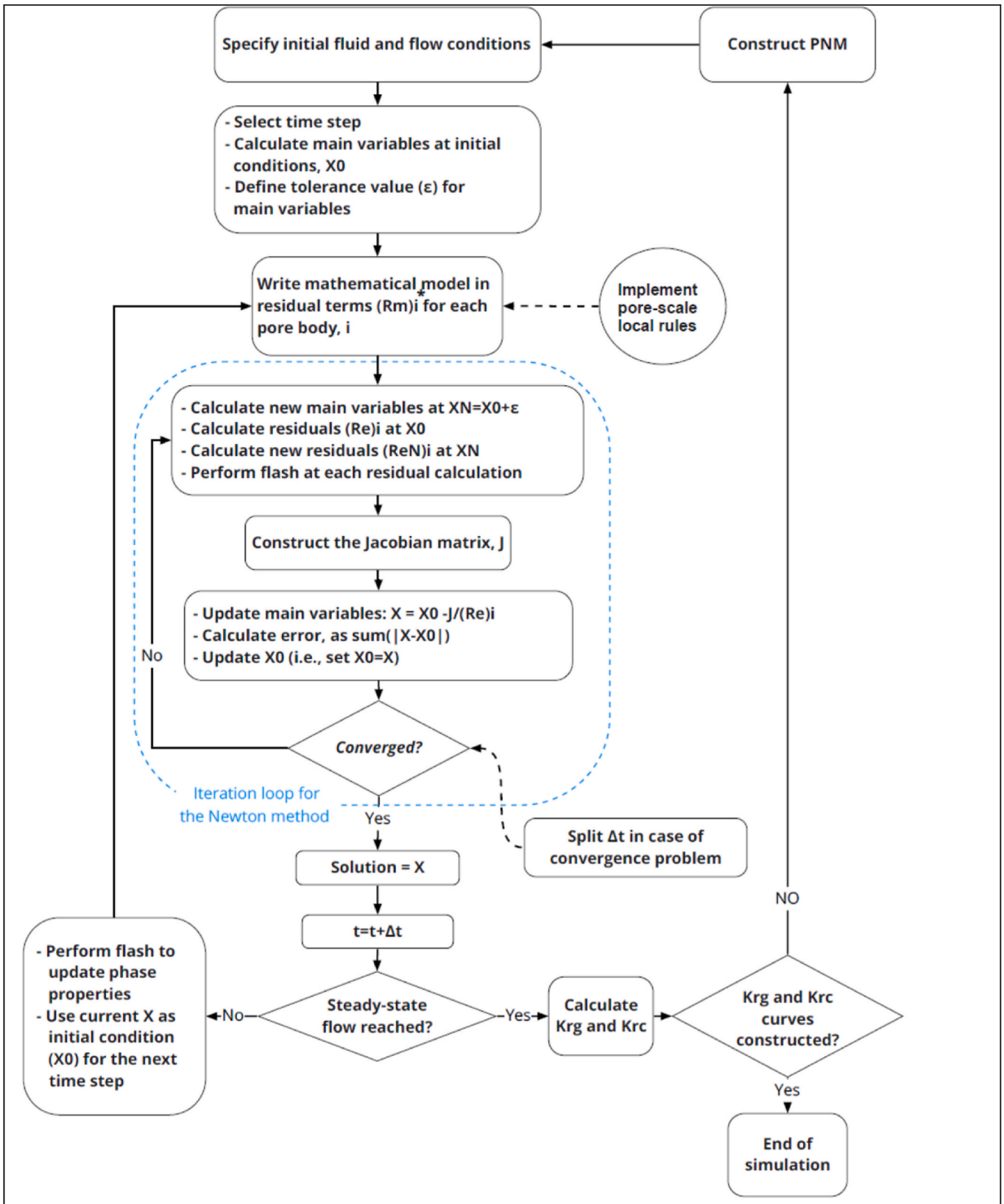

* $(R_m)_i$ = [Summation of molar rates at each pore body node, i] + [+inlet/-outlet molar rates at the boundary] – [molar change for each control volume versus time]

Fig. 9. The flowchart of the applied dynamic compositional pore-network model used for the simulation of gas-condensate flow.

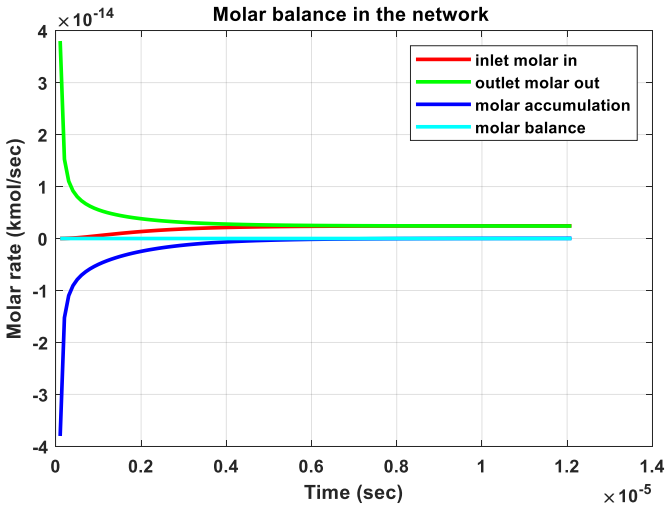

Fig. 10. 3D pore network molar consistency representing the accuracy of implemented numerical model.

Numerical problems arise when a phase emergence or vanishment happens, which can cause less numerical convergence and oscillations during Newton method iterations (Weishaupt and Helmig, 2021). Possible remedies have been reported in previous studies by Class et al. (2002), introducing a switching strategy for a set of primary variables of the solution method and also, by Lauser (2014), Lauser et al. (2011), Weishaupt and Helmig (2021), implementing a more stable approach with fixed primary variables but with an extra constraint equation to be solved for phase saturations. In this work, the case of simulations is within the two-phase region with no abrupt compositional change, thereby, such numerical problems are not encountered. The macroscopic flow terms, such as relative permeability values, are calculated when the steady-state flow condition was established along the pore network using Darcy's law. The flowchart for the simulation of dynamic gas-condensate flow in the pore network implementing the proposed mathematical model is shown in Fig. 9. The above approach is similar to the algorithm proposed by Chen ate al. (2020) where a fully implicit algorithm was applied, and the main variables (i.e., pressure, saturation and composition) were simultaneously solved within each time step using Newton iterations. However, we could not directly employ their results for comparison due to differences in composition, saturation range, research focus (gas-condensate flow in our study vs. viscous fingering in Chen et al. (2020)), and model types (bond model in our study vs. pore-site model in Chen et al. (2020)).

3.9. 3D model assessment and verification

3.9.1. Molar balance check

The molar consistency equation for the whole network was first examined in each time step to inspect the numerical model accuracy. Fig. 10 presents the molar conservation across the whole network during one of the 3D simulations. When the inlet total molar rate of the system approaches the outlet total molar rate, the average pressure along the network tends towards a constant value at which the network outlet flow rates are calculated to obtain the relative permeability curve.

3.9.2. Comparison with experimental data

To validate the model, the results of the 3D PNM simulations were compared with experimental data available in the literature for the liquid-wet medium. The 3D pore-network model was constructed to have an absolute permeability as the initial conditions of the experiments. Next, the compositional gas-condensate flow was set up to simulate different velocity levels and fluid IFTs, reported at experimental conditions (Jamiolahmady et al., 2003). It is worth noting that

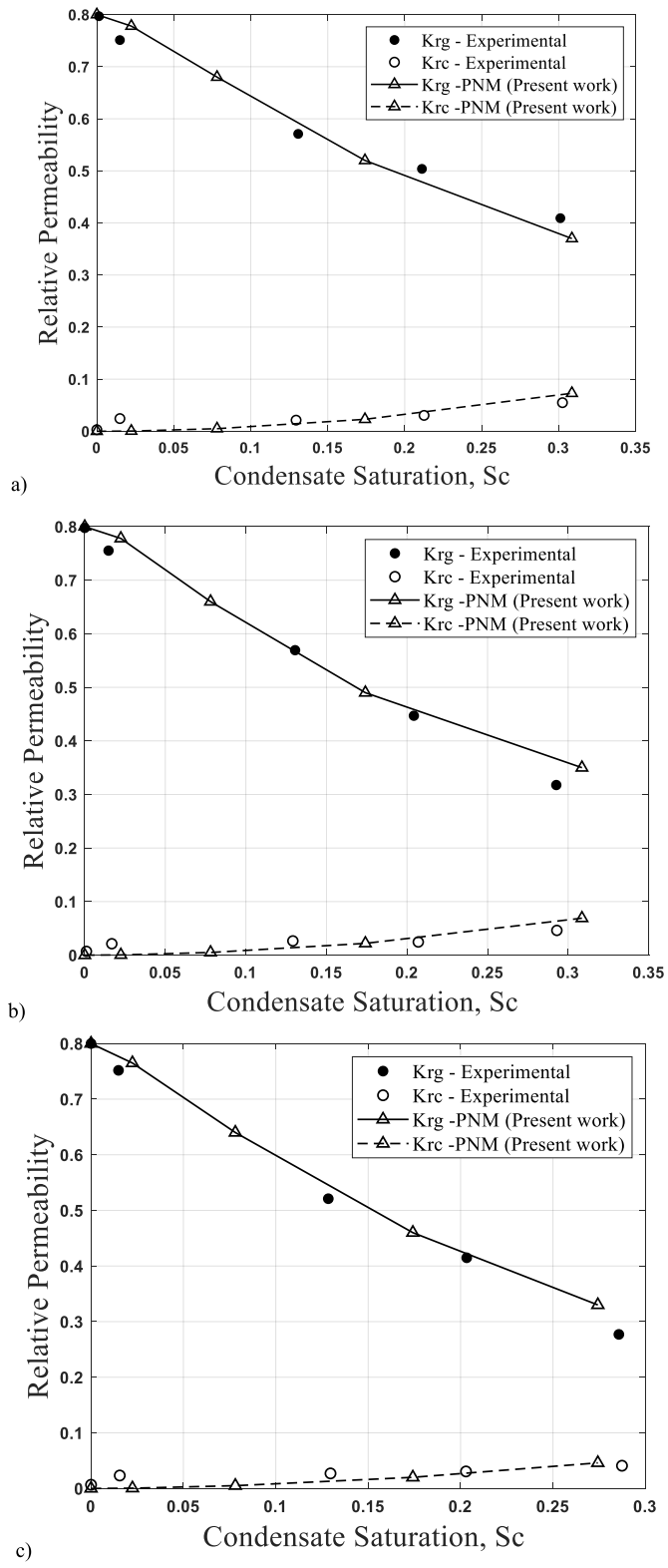

Fig. 11. 3D PNM and experimental (Jamiolahmady et al., 2003) gas and condensate relative permeability at IFT = 0.015 mN/m and constant velocity of a) 36 m/day, b) 18 m/day and c) 9 m/day.

required model parameters were measured and obtained from experiments performed by previous studies, allowing us to implement and use them in our model (for example, the average coordination number, Z, was taken from CT images of Berea Sandstone). Furthermore, to compare the simulations with experimental results, all simulations have

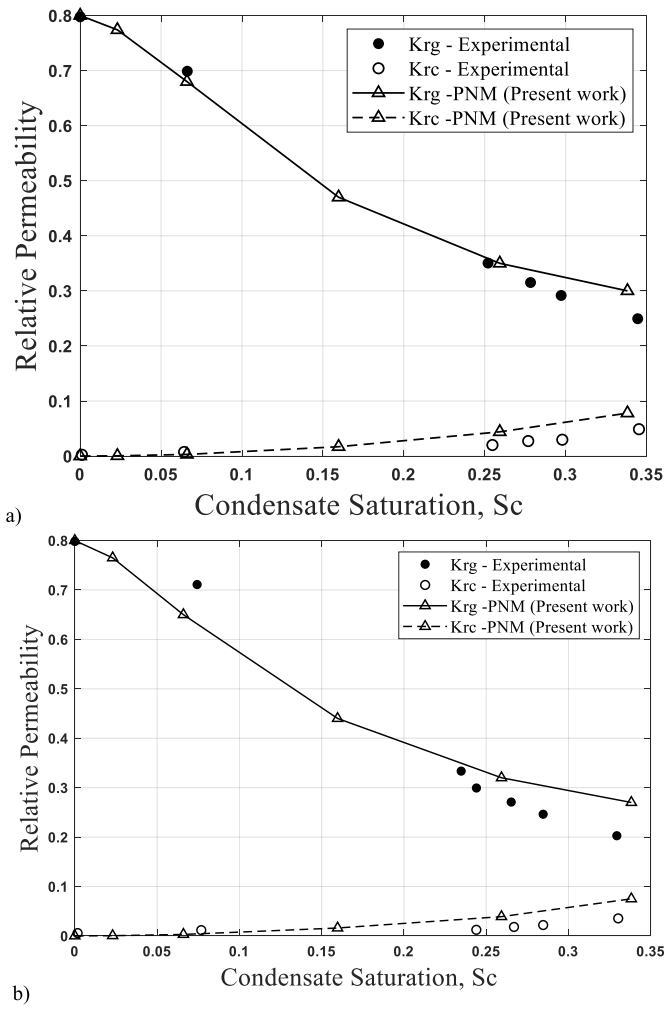

Fig. 12. 3D PNM and experimental (Jamiolahmady et al., 2003) gas and condensate relative permeability at IFT = 0.037 mN/m for a) constant velocity of 36 m/day and b) constant velocity of 18 m/day.

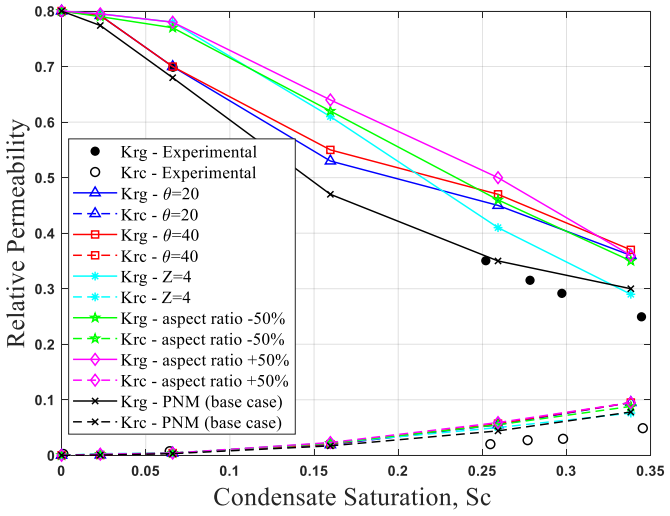

Fig. 13. Sensitivity analysis of the 3D PNM model parameters: the effects of contact angle, coordination number and aspect ratio on the gas-condensate relative permeability as compared to the experimental data (Jamiolahmady et al., 2003) at IFT = 0.037 mN/m for constant velocity of 36 m/day.

been conducted with triangular shapes for modeling Berea sandstone within condensate saturation range of 0%–35% encompassing the experimental data points for the considered composition, temperature, and pressure.

As shown in Figs. 11 and 12, a fairly reasonable agreement has been achieved between the 3D model and core-flood experiments reported by Jamiolahmady et al. (2003). To further examine the model validity, several model parameters have also been selected to analyze their effect on the 3D model results. The effect of aspect ratio, contact angle and coordination number on the gas-condensate relative permeability in 3D models was analyzed and compared with the experimental results (Fig. 13), which shows the adequacy and accuracy of the selected values for these model parameters. As can be seen, any change in the average coordination number, Z, contact angle as well as aspect ratio results in a deviation of prediction from the experimental data and less accuracy of the predictions. Further analysis of the 3D results is discussed in the next section.

4. Simulations results and discussions

4.1. 3D model results: comparison with other studies

Fig. 14a and Fig. 15a compare the IFT effect on relative permeabilities; in higher IFTs, the Jamiolahmady et al. (2003) model did not have a good match for condensate saturations above 25% (showed a sharp decrease in K_{rg} and a sharp increase in K_{rc}), while the Reis and Carvalho's (2021) model overestimated the K_{rg} in saturation range below 25% and had an acceptable match at higher condensate saturations above 25%. Their K_{rc} simulated values were also overestimated in comparison to experimental data. In our model, K_{rc} and K_{rg} are almost in line with experimental data, but at saturations above 25%, which is not in the practical range, they are overestimated.

At the velocities of 36 m/d and 18 m/d, looking at Fig. 14a and b as compared to Fig. 15a and b, the IFT had a pronounced adverse effect on K_{rg} and K_{rc}. The reason was due to the higher capillary force effect on the entrapment of condensate in the restriction capillaries. Comparing Fig. 14(a–c) and Fig. 15(a–b), the positive impact of velocity on K_{rg} and K_{rc} was appreciable, especially for the K_{rg}.

At an IFT of 0.015 mN/m, the results of Reis and Carvalho's model (2021), did not have a good match with experimental data for both K_{rg} and K_{rc} curves. There was an overestimation of K_{rg} for the condensate saturations below 25% and K_{rc} at condensate saturations between 15% and 30%. This controversy can be attributed to the effect of the annular flow of condensate as a thin layer of liquid along the capillary walls with a converging-diverging profile, due to which each phase was expected to flow freely (i.e., the friction of pore walls and fluids does impact the flow, and moreover, the effect of angularity on the throat conductance has not been considered in their study).

The pore-network model of Jamiolahmady et al. (2003) showed a fair match with experimental at lower velocities for lower IFTs. Additionally, at higher IFTs, their model failed to get a fair match with K_{rg} and K_{rc}, especially at condensate saturations above 25%.

The comparison of the performance between our model, previous models and experimental results indicates that the discrepancy in results can be attributed to several factors including the pore-network representations, assumptions, governing equations, numerical algorithms, and other unrepresented rock sample characteristics (e.g., irregular pore shape, mixed wettability, etc.). In terms of pore-network representation, for instance, Jamiolahmady et al. (2003) considered circular-shaped pores with a constant outlet radius/inlet radius ratio for all pores. They have also introduced the equivalent pore throat length as an additional geometrical parameter to account for the effect of flow resistance and pore tortuosity on gas-condensate flow. On the other hand, Reis and Carvalho (2021) considered the converging-diverging pore geometry, in which the condensate phase was distributed either as a thin film on the surface of pore throats or a condensate bridge

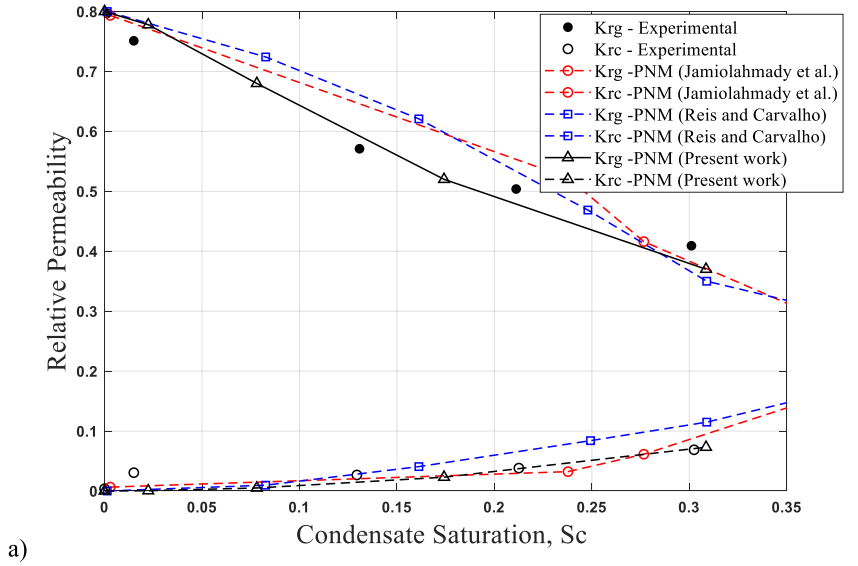

a)

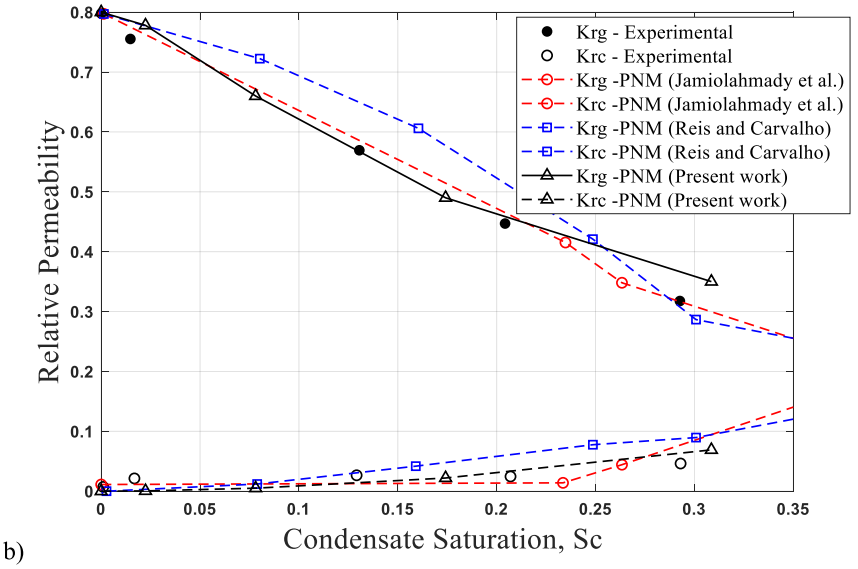

b)

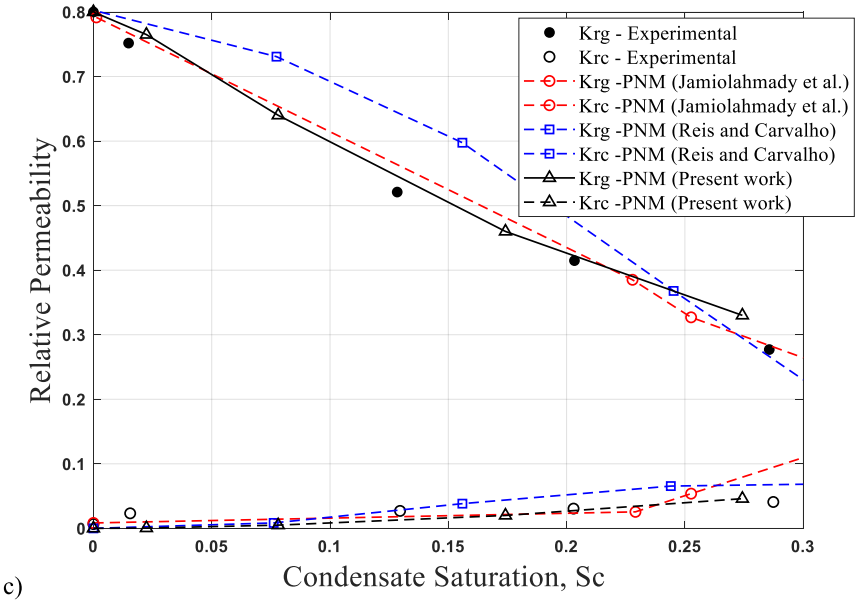

c)

Fig. 14. 3D PNM gas and condensate relative permeability curves and experimental data (Jamiolahmady et al., 2003) at IFT = 0.015 mN/m and constant velocity of a) 36 m/day, b) 18 m/day and c) 9 m/day.

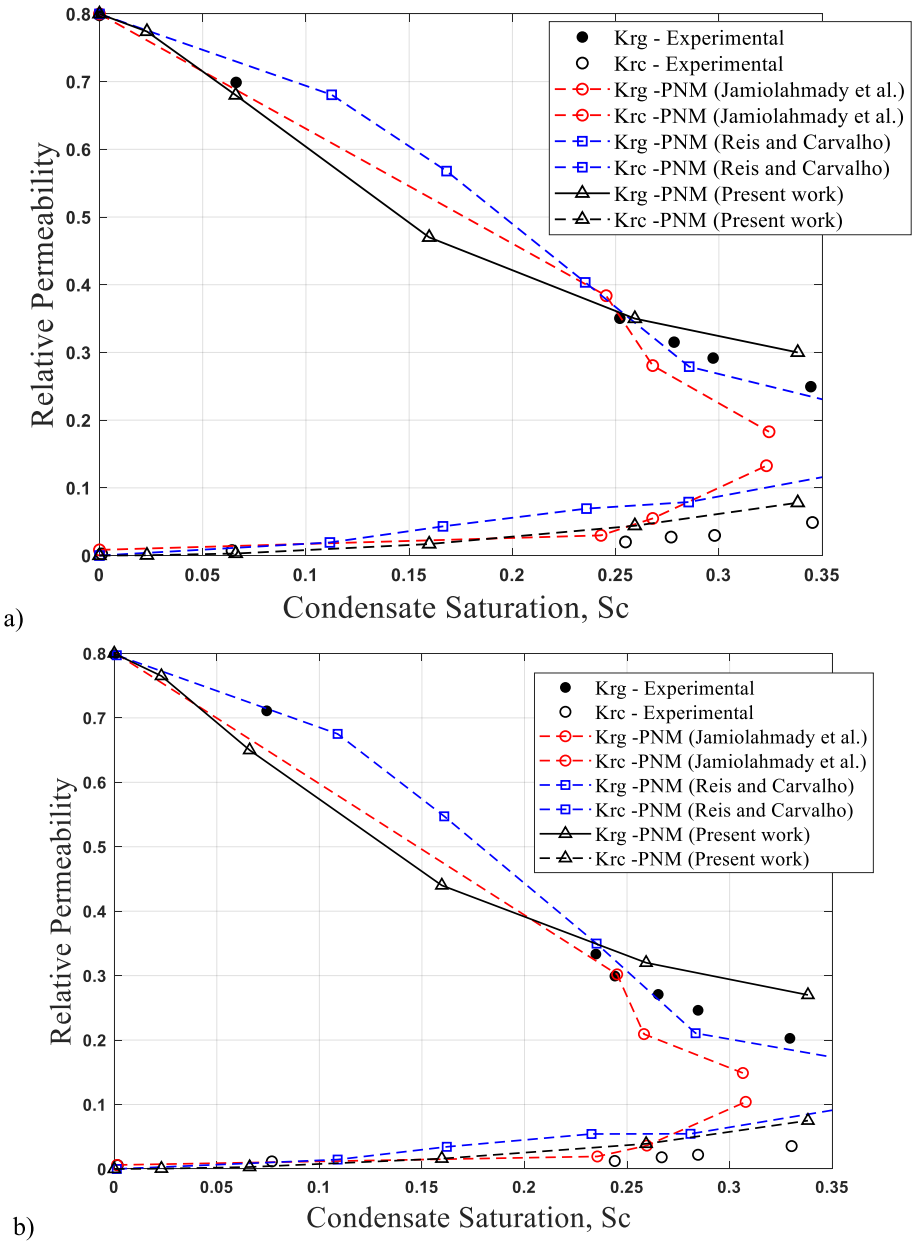

Fig. 15. 3D PNM gas and condensate relative permeability curves and experimental data (Jamiolahmady et al., 2003) at IFT = 0.037 mN/m for constant velocity of a) 36 m/day and b) 18 m/day.

accumulated at the pore throat mid-section during snap-off conditions. In the current study, however, a pore network representation based on the pore shape factor distribution available for a Berea sandstone samples has been used, for which angular cross sections have been utilized. Angular shapes used for modeling Berea sandstone in this study could provide a better representation of the pore space than the circular cross-sectional shapes employed by Jamiolahmady et al. (2003) and Reis and Carvalho (2021). As snap-off mechanism, which controls the gas-condensate flow phenomena (i.e., through the cycle of condensate blockage and mobilization), is manifested more markedly in angular shapes. Therefore, it seems that pore morphology plays a great role through its influence on fluid phase conductance and snap-off criteria. Given the importance of pore morphology, therefore, this study presents a comprehensive parametric study inclusive of pore morphology effects on the gas-condensate flow, accounting for different rock porous geometries.

The current model demonstrated strong predictive ability for gas-condensation systems' K_{rc} curves, particularly at saturations up to 30%, which are common in gas-condensate reservoirs. The condensate relative permeabilities matched experimental results well due to the incorporation of the friction factor beta, which effectively accounted for the wetting phase's corner flow in angular-shaped capillaries, assuming a free boundary between the gas and condensate interface. The proposed model yielded improved predictions, particularly in low interfacial tensions (IFTs), owing to the effect of pore shape angularity on throat conductance and snap-off, which were not considered in Reis and Carvalho's (2021) model. Additionally, the developed PNM leveraged a compositional algorithm (molar conservation) to provide better estimates of condensate creation and associated snap-off processes compared to Jamiolahmady et al.'s (2003) model.

Moreover, analysis of the average statistics of blocked throats due to condensate formation at various condensate saturations under different velocities and IFTs confirmed the facilitating effect of velocity on blockage removal and the contribution of capillarity (higher IFT) to

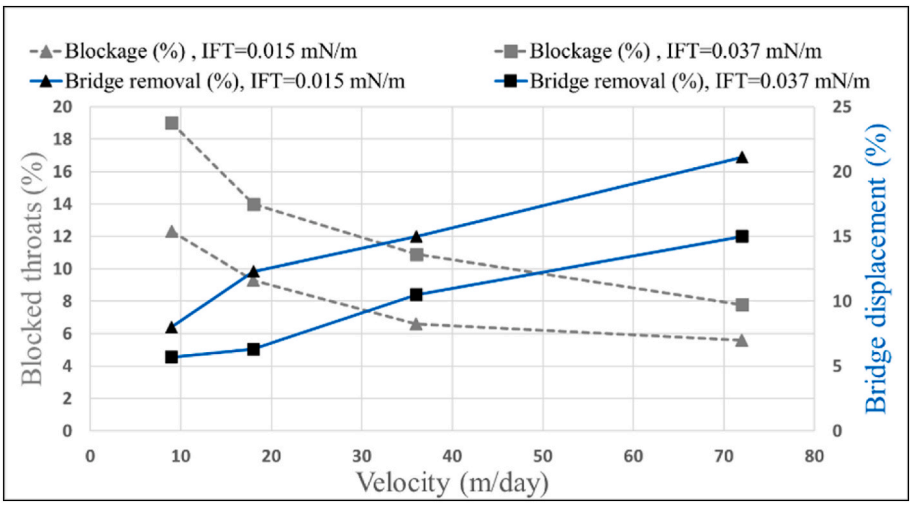

Fig. 16. The results of 3D simulations showing the effect of velocity and IFT on degree of condensate blockage and viscous force contribution in displacement of condensate bridges in pore throats.

condensate blockage (see Fig. 16).

4.2. 2D model results

Fig. 17 presents the effect of 2D network size on the relative permeability values. As can be seen, the network size has little impact on gas relative permeabilities beyond 25 × 25 × 1 networks. Under fixed wettability and flow conditions, our selected 2D network model dimensions have proven sufficient and representative for parametric analysis.

Fig. 18 illustrates the distribution of throat size, condensate saturation, and condensate blockage (i.e., the condensate bridges that cannot be mobilized by the gas viscous flow; H = 0) in the throats of the pore network at steady state flow conditions. The condensate bridges that can be mobilized by the viscous gas flow, would flow eventually into the corresponding control volume at the considered node, then the saturation of the throats in the specified control volume would be updated based on the molar balance of the wetting phase (condensate) at that control volume (please see section 3.5). In the following, the sensitivity analysis of the major interacting parameters of gas-condensate flow is presented.

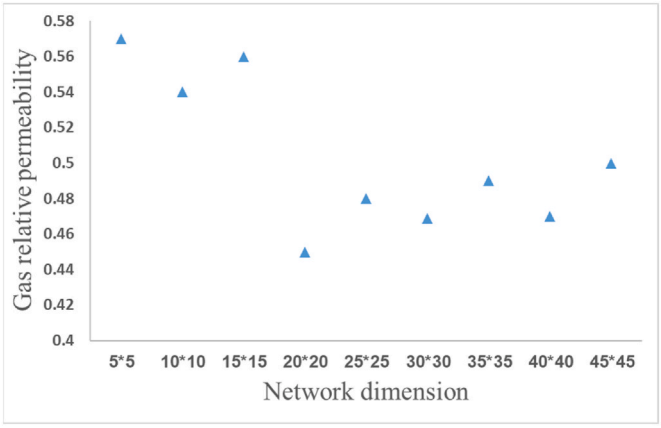

Fig. 17. The effect of 2D network dimension on gas relative permeability at Sc = 16.9%, IFT = 0.037 mN/m, pore shape of triangle, contact angle = 0, and velocity of 36 m/day.

4.2.1. The effects of pore shape and IFT on gas-condensate relative permeability

At the same fluid velocity level, Fig. 19a indicates that the square throat cross-section exhibited the lowest gas and condensate relative permeability compared to the triangular and circular-shaped throats. This effect can be attributed to the snap-off process, which occurs at lower condensate saturations for square cross-sectional throats. As a result of snap-off, the reduction in gas relative conductivity occurs at lower condensate saturations. The relative permeabilities of triangular shapes were closer to the results of PNMs with circular-shapes cross sections than the PNMs with the square cross section due to the proximity of the limiting condensate saturation controlling snap-off. The limiting condensate film thickness for snap-off was set to 0.25 R t (equivalent to a condensate saturation of 43.75%) for cylindrical throats. For throats with triangular cross-sections, the condensate blockage occurred around a condensate saturation of 40% (i.e., the saturation at which the wetting condensate phase swells towards the center of the pore throat).

Bustos and Toledo (2004) analyzed the pore shape effect (i.e., angularity) on gas-condensate relative permeabilities for triangle, square, and octahedron cross-sections using pore-network modeling. However, they did not consider near-wellbore regions and only accounted for the capillary and gravity forces. In the current model, the square-shaped throats exhibited more blockage at relatively lower condensate saturations simulated under dynamic flow conditions.

Another important factor governing the decline of gas and condensate relative permeability at the same condensate saturation was the interfacial tension (IFT). The effect of IFT on relative permeability is rooted in its presence in the definition of entry pressure for a given throat, which is a function of pore geometry, IFT, and contact angle. In a strongly liquid-wet medium, higher values of IFT at lower reservoir pressures cause the capillary force to maintain the condensate bridges in the narrowest capillaries, blocking a greater portion of gas flow paths. The negative effect of IFT was also pronounced for the condensate relative permeability, as a lower number of throats contribute to the flow of condensate. At lower condensate saturations, relative permeability curves were similar for different shapes at the same pore size distributions because the number of blocked throats due to snap-off is small, having a minor impact on the relative permeabilities. Fig. 19b shows that the IFT has almost no effect on the relative permeability of gas and condensate at a contact angle of 90° (i.e., neutral wettability) for all investigated pore shapes. The reason is that the blocked throats are already displaced by the gas phase at contact angles close to 90°. Additionally, the contribution of viscous force in the absence of a high

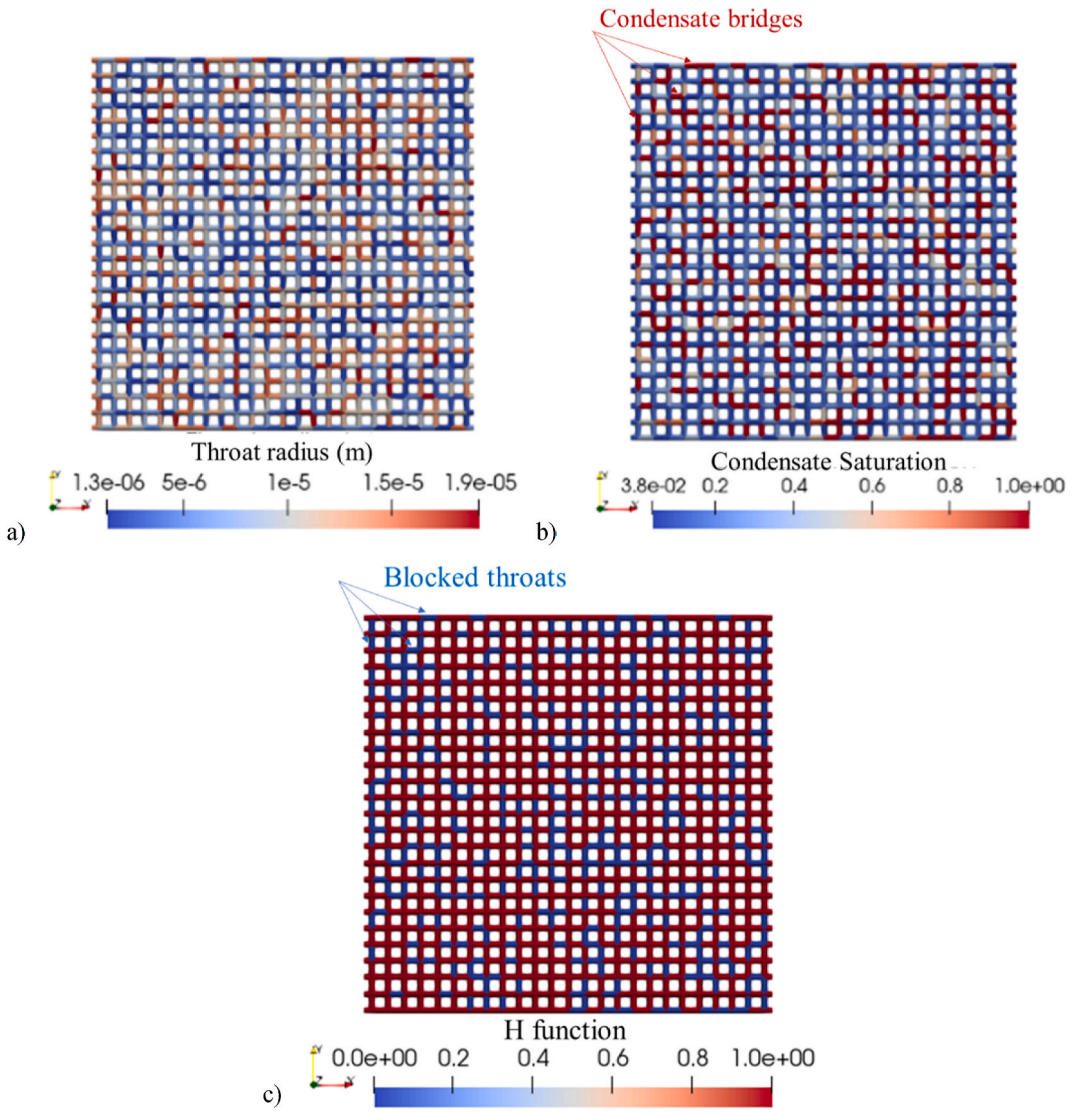

Fig. 18. 2D PNM simulations (triangle pore shape): a) 2D throat size, b) the condensate saturation distribution of the 2D model representing c) the distribution of blocked throats as a result of condensate creation and snap-off mechanism (pore network average S_c = 15.9% at the steady state condition).

capillary force effect led to the movement of the condensate bridges mostly along the network (lower blockage) in neutral wettability. On the other hand, the angularity effect on the reduction of relative permeabilities was found to be less for neutral wettability.

4.2.2. The effects of pore shape, contact angle and IFT on gas-condensate relative permeability

Fig. 20(a–c) shows the influence of pore shape and wettability on the relative permeabilities at different IFTs. The wettability alteration, almost in all cases, had a positive effect on the relative permeability of both phases. Our results are consistent with the results obtained for the improvement effect of wettability change investigated by Li and Firoozabadi, 2000 in a phenomenological model studying gas condensation. Bustos and Toledo (2003) also approved the positive effect of wettability change to the intermediate wetting on gas-condensate relative permeabilities at the condensate saturations above 20% through their 3D pore-network model with square cross-section capillaries under the just contribution of capillary and gravity force (i.e., not considering the viscous effects, dominant in near wellbore region and not from a dynamic PNM approach). In our parametric study, the wettability effect was more substantial at the highest IFTs and more pronounced on gas relative permeability than condensate relative permeability regardless of pore shape.

Fig. 21(a–c) presents the influence of IFT and contact angle on relative permeabilities for different throat shapes. The wettability effect was more beneficial at higher IFTs, and it was seen that its effect on the relative permeabilities is relatively higher for square and triangular-shaped throats, and more noticeable at higher condensate saturations (higher than 15%). The negative effect of IFT on the gas and condensate relative permeabilities was stronger for the square cross-section because a larger number of throats are blocked and could not be opened to gas flow. The contact angle change was also effective almost in a wide range of condensate saturations and its effect was more pronounced in angular cross-section throats. The wettability effect for each pore shape at IFT of 0.04 mN/m and velocity of 35 m/day was shown in Fig. 22(a–c). The higher the contact angle was, the higher the gas relative permeability would become, particularly for the values of contact angle close to the corner angle of angular-shaped throats (this pattern is much more

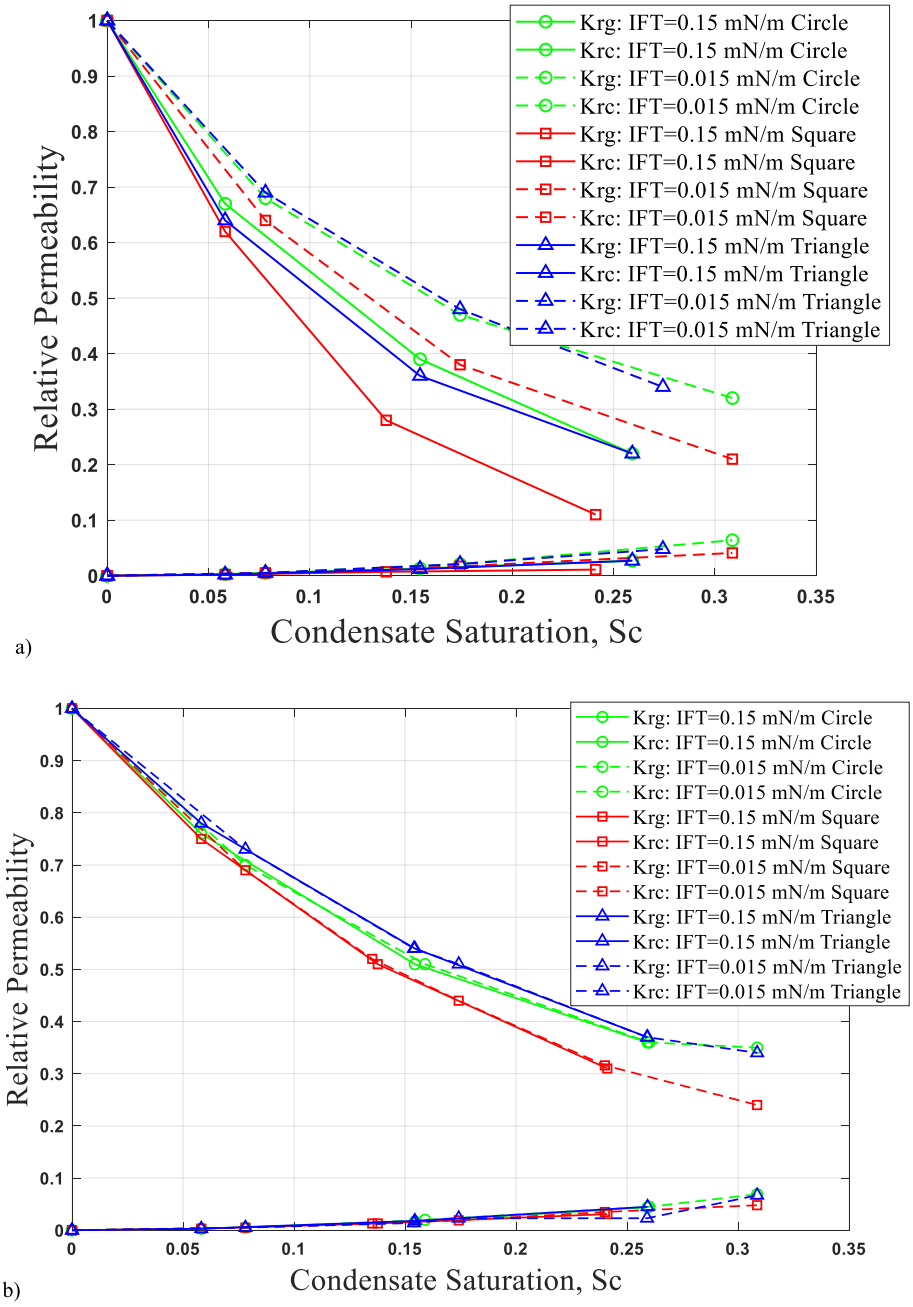

Fig. 19. 2D PNM Gas and condensate relative permeability curves at constant velocity of 35 m/day for a) liquid-wet medium and b) neutral-wettability medium.

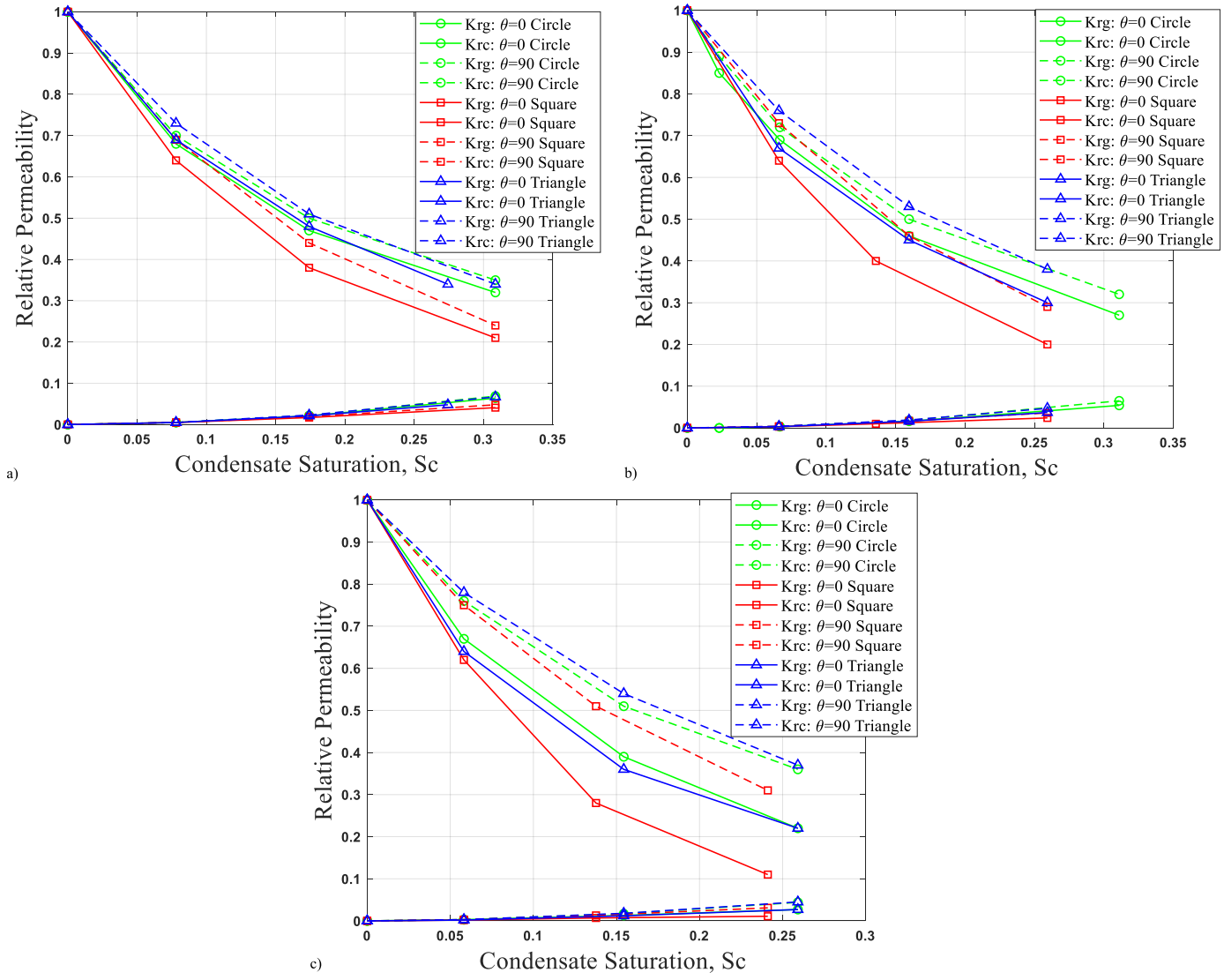

Fig. 20. 2D PNM Gas and condensate relative permeability curves at constant velocity of 35 m/d for a) IFT = 0.015 mN/m, b) IFT = 0.04 mN/m and c) IFT = 0.15 mN/m.

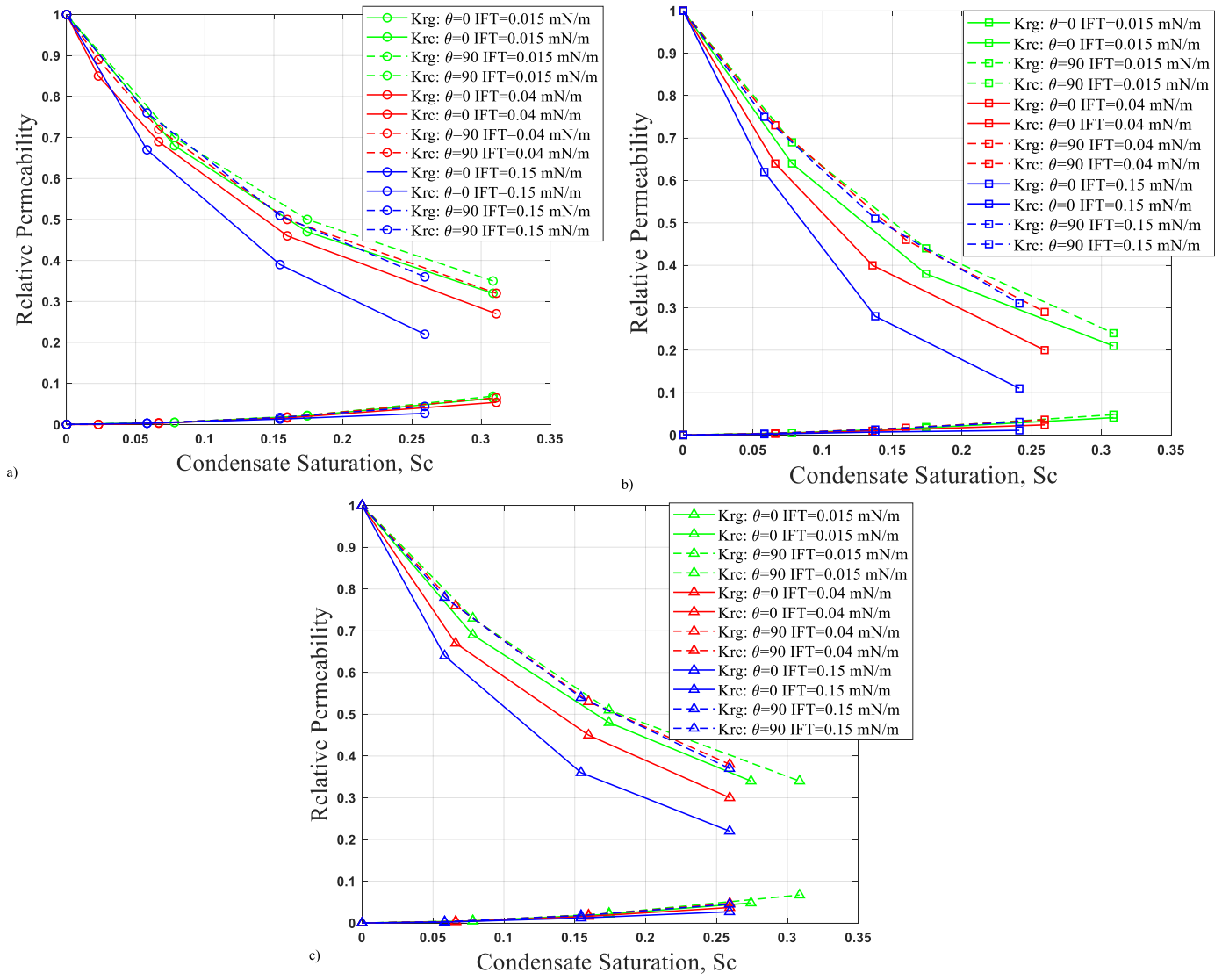

Fig. 21. 2D PNM Gas and condensate relative permeability curves at constant velocity of 35 m/day for throat geometry of a) circular cross-section, b) square cross-section and c) triangular cross-section.

appreciable in the square cross section). Additionally, based on the average statistics of the opened throats to the gas flow and condensate bridge displacements presented in Fig. 23 confirms the positive effect of wettability on blockage removal, and the contribution of capillary force (higher IFT) on the condensate blockage.

4.2.3. The effects of velocity and IFT on gas-condensate relative permeability

Fig. 24(a–c) illustrates the relationship between relative permeabilities and various velocities and interfacial tensions (IFTs). The positive effect of velocity is more pronounced at higher IFTs and elevated condensate saturations. This is because a greater pressure gradient, associated with higher velocity levels, aids in the mobilization of condensate bridges under increased gas phase pressure. The impact on gas relative permeability becomes more apparent due to the increased number of condensate bridges at higher condensate saturations. Conversely, at lower condensate saturations, there are fewer blocked throats, resulting in a minimal increase in phase permeabilities as velocity increases. The effect of velocity change on condensate relative permeability is less significant than its impact on gas relative permeability. This is because velocity changes primarily open gas pathways in the blocked throats, which considerably influence gas relative permeability. In contrast, condensate relative permeability is associated with condensate thickness and the contribution of corner condensate flow, both of which are minimally affected by velocity changes. Instead, these factors are largely governed by pore shape and wettability.

5. Summary and conclusions

A 3D dynamic compositional PNM, featuring an efficient algorithm for coupling phase equilibrium and two-phase flow, was developed to model the gas-condensate flow in conventional reservoirs. Furthermore, a fully implicit algorithm was employed to simulate gas-condensate flow in conjunction with phase equilibrium calculations. The response surface methodology (RSM) was utilized to approximate phase properties as linear functions with high precision, accelerating simulations and enhancing the computational speed of Newton's iterations. The 3D model's results aligned with experimental data from Berea core flood experiments, demonstrating the proposed computational algorithm's reasonable accuracy. A novel approach was introduced to determine condensate saturation in throats based on liquid mole count and throat size order. Considering corner conductivity for the condensate phase resulted in improved condensate relative permeability predictions compared to prior research. To minimize computational costs of

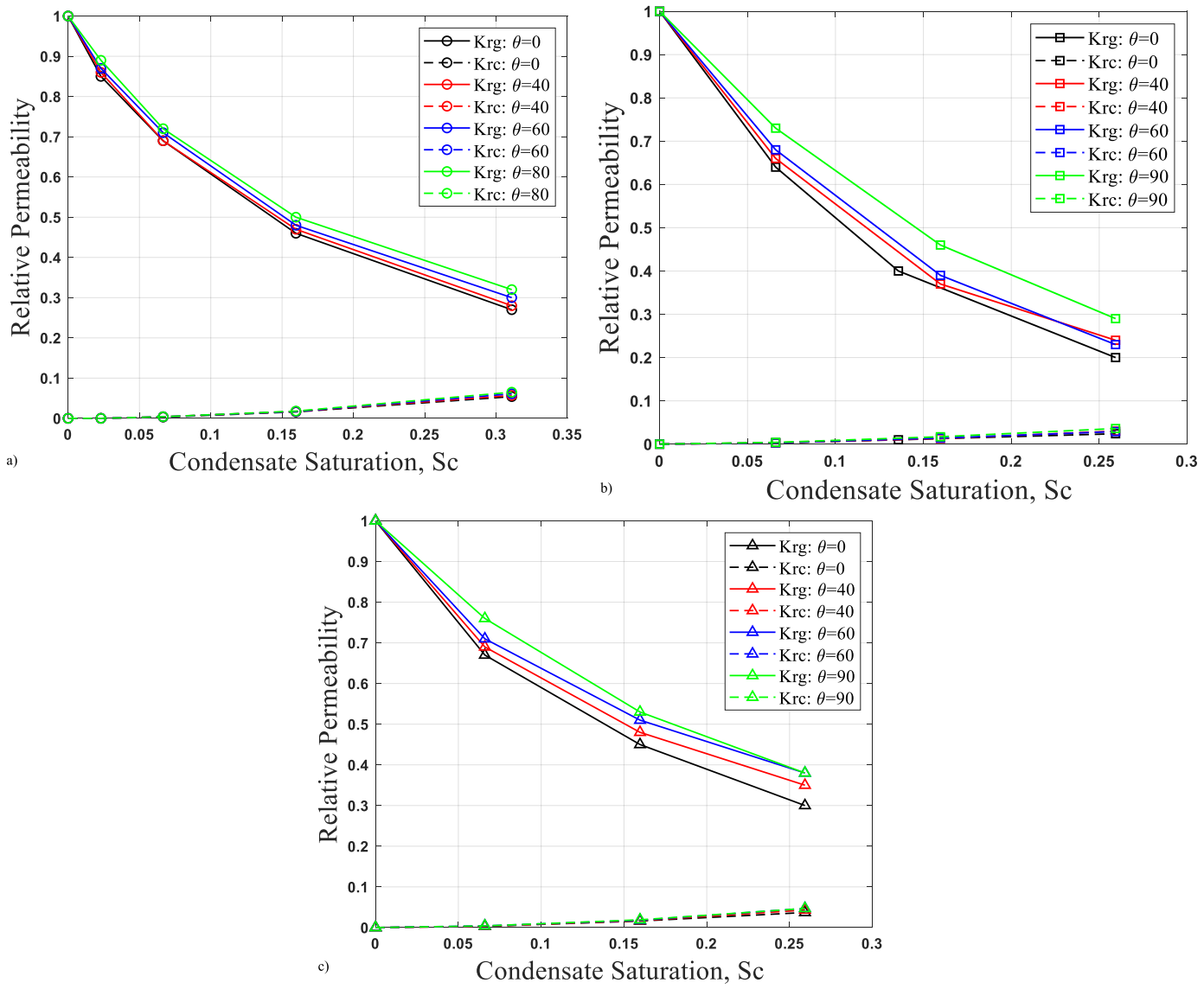

Fig. 22. 2D PNM Gas and condensate relative permeability curves at IFT = 0.04 mN/m and constant velocity of 35 m/d for throat geometry of a) circular cross-section, b) square cross-section and c) triangular cross-section.

extensive parametric studies requiring multiple dynamic compositional pore-network models, 2D models were used to examine retrograde condensation in porous media without gravity effects across three pore shapes.

The parametric study revealed that altering wettability to intermediate and neutral wetting in angular pore geometries significantly mitigated condensate blockage, particularly under higher IFTs. This improvement was most evident in gas relative permeabilities at increased condensate saturations. Gas relative permeability noticeably decreased at the highest IFTs due to snap-off and the intensifying capillary force constricting condensate bridges in throats. Square-shaped throats exhibited the lowest gas-condensate relative permeabilities as snap-off occurred at lower condensate saturations. Additionally, simulations revealed the positive coupling rate effect (i.e., the positive influence of velocity and the negative impact of IFT). The velocity effect was predominantly pronounced at larger interfacial tension values, while the IFT impact was minimal under neutral wetting conditions.

6. Outlook for the future studies

This study's findings highlight the importance of pore geometry and rock petrographic types in condensate recovery. A more comprehensive analysis of pore shape (shape factor) and wettability's influence on gas-condensate relative permeabilities necessitates extending pore-scale visualization and imaging of transport phenomena in gas condensation systems. However, this requires the development of a high-pressure experimental setup and tailored imaging facilities. Until then, the established compositional pore-network model can act as a numerical experiment, illuminating the effects of various governing factors.

The suggested procedure can be integrated into future research examining gas-condensate flow in unconventional reservoirs such as shales. However, it must accommodate specific characteristics of these media, including organic matter presence (see e.g., Yu et al., 2020), nanopore flows, multiscale pore structures (Yu et al., 2018, 2019, 2021), capillary effects on phase equilibrium (Song et al., 2020), and other relevant processes and phenomena for unconventional reservoirs. Finally, the development of hybrid pore scale models, that is the use of pore-network models for simulating gas-condensate flow, incorporating the advanced numerical schemes such as phase field-based lattice Boltzmann for better characterization of condensate bridge coalescence at the pore scale (see e.g., Younes et al., 2022) can be considered as another direction for future studies.

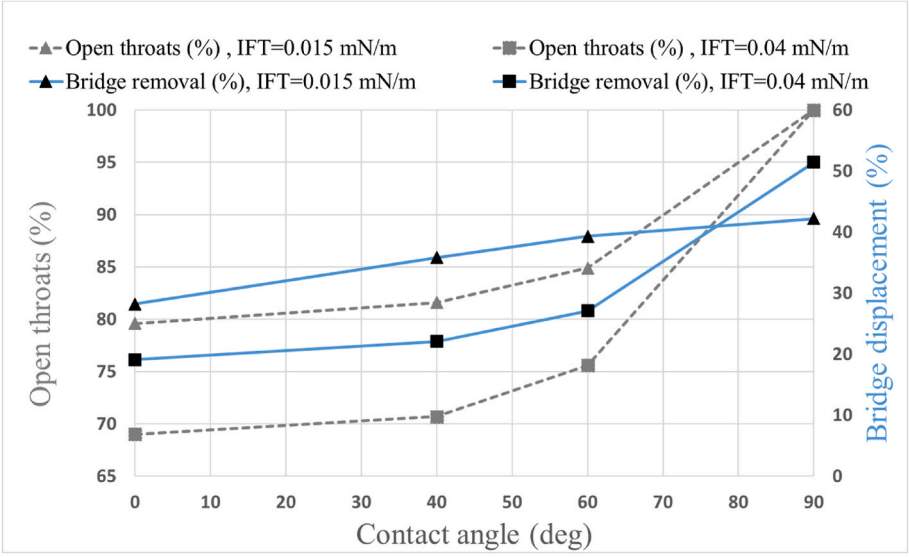

Fig. 23. 2D PNM (with square shaped throats): the effect of contact angle and IFT on the average percentage of throats open to gas flow and condensate bridge displacement.

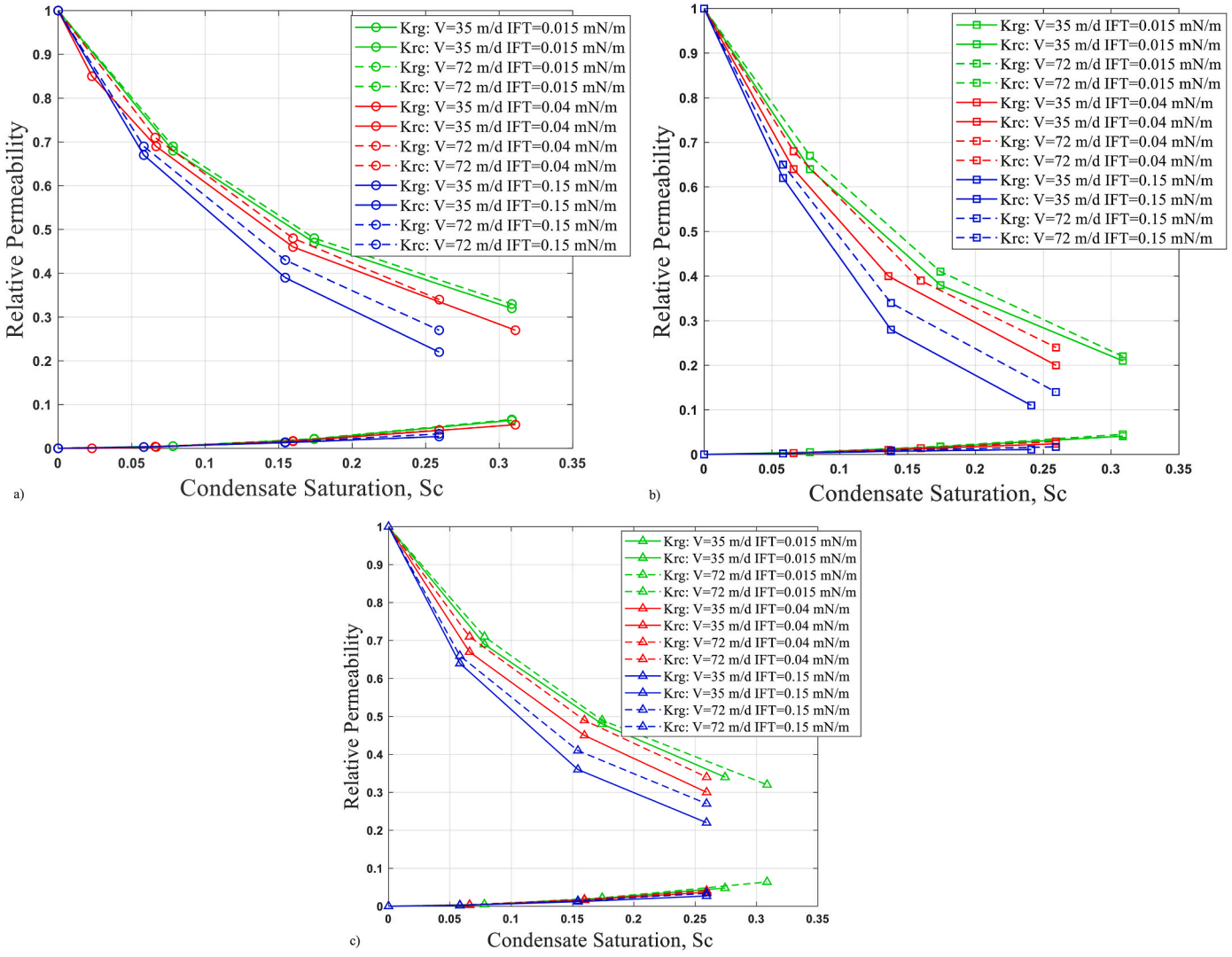

Fig. 24. 2D PNM Gas and condensate relative permeability curves at liquid-wetting conditions for a) circular cross-section, b) square cross-section, and c) triangular cross-section.

Credit author statement

A. Hosseinzadegan: Conceptualization, Methodology, Programming, Simulations, Data Analysis and Interpretation, Writing-Original draft preparation. Writing-Reviewing and Editing. **H. Mahdiyar:** Supervision, Conceptualization, Methodology, Model Development, Data Analysis and Interpretation, Validation, Writing-Original Draft Preparation, Writing-Reviewing and Editing. **A. Raoof:** Supervision, Methodology, Data Analysis and Interpretation, Writing-Reviewing and Editing. **Ehsan Nikooee:** Advisor, Conceptualization, Methodology, Data Analysis and Interpretation, Writing-Original Draft Preparation, Writing-Reviewing and Editing. **Jafar Qajar:** Advisor.

Declaration of competing interest

The authors declare that they have no known competing financial interests or personal relationships that could have appeared to influence the work reported in this paper.

Data availability

Data will be made available on request.

Acknowledgement

The authors would like to thank the constructive comments of three anonymous reviewers as well as Dr. Paula Reis of the University of Oslo for fruitful discussions on different aspects of compositional pore-network modeling in the course of this study.

Nomenclature

A	area
D	referring to the height
f	fluid
f	fugacity
g	fluid conductance
G	shape factor
H	step function showing the status of opening or closing of a capillary for flow
H_{ij}	step function specifying the opening or blockage status of a throat
H^e	step function specifies the status of bridge displacement in a throat
K_i	ratio of gas molar fraction to the liquid molar fraction
K_{rc}	condensate relative permeability
K_{rg}	gas relative permeability
l	throat length
L	Liquid
m	mass
n_c	number of corners
n_c	number of components
n_L	liquid molar fraction
n_V	vapor molar fraction
N	number of moles
N_{cap}	number of connecting throats to a pore body
P	pressure
P_c	capillary pressure
P_e	entry pressure
ΔP	pressure gradient
ΔP^e	pressure gradient needed to mobilize the condensate bridge snapped-off in the throat
Q	flow rate
r_1	the radius of curvature for the condensate meniscus at a specified saturation
R_t	inscribed radius of the throat
R	throat radius
S	fluid saturation
t	time
Δt	time step
t_{crit}	the condensate thickness at which the condensate film gets snapped off in a throat
T	transmissibility term
V	volume
x	index for the liquid molar fractions
y	index for the gas molar fractions
Z	mixture molar composition

Greek Symbols

α	corner half angle
β	resistance factor
θ	contact angle
θ_r	receding contact angle

φ	fluid potential
μ	fluid viscosity
φ	porosity
ρ	fluid density
σ	gas-condensate interfacial tension
v	molar velocity
τ	iteration number

Subscripts

c	corner
crit	critical
entry	referring to entry pressure
g	index for the gas phase
i	property in pore body node i
j	property in pore body node j
in	inlet
ij	index for the capillaries
l	index for the condensate liquid phase
m	component
out	outlet
r	receding

Superscripts

e	entry
g	gas phase
l	liquid phase
n	time counter
t	time

Abbreviations

2D	two dimensional
3D	three dimensional
AR	aspect ratio
C_1	methane
nC_4	normal butane
EOS	equation of state
IFT	interfacial tension
LBC	Lohrenz-Bray-Clark (Lohrenz et al., 1964)
MTM	main terminal meniscus
PNM	pore-network model
RSM	response surface method

Appendix A. Derivation of molar conservation equation

The conservation law can be applied over a specified control volume, V_i by definition of fluids flow through each face of its body. Considering molar flow rates, the material balance is written for all components in the fluid mixture, entering or exiting the control volume with respect to time, Δt as the following expressions:

Entering molar flow − Exiting molar flow + Source/sink terms = Accumulated molar term

$$\text{The number of moles of each component entering the system} = \left(\sum_{ij}^{Ncap} N_{m,ij}\right)_{in} \Delta t \quad ;\mathrm{m} = 1\ldots n_c \tag{A.1}$$

$$\text{The number of moles of each component exiting the system} = \left(\sum_{ij}^{Ncap} N_{m,ij}\right)_{out} \Delta t \quad ; m = 1\ldots n_c \tag{A.2}$$

$$\text{Accumulated molar term} = V_i\left(S_l x_m \overline{\rho}_l + S_g y_m \overline{\rho}_g\right)^{t+\Delta t} - V_i\left(S_l x_m \overline{\rho}_l + S_g y_m \overline{\rho}_g\right)^{t} \tag{A.3}$$

$$-\sum_j^{N_{cap}}\left[\left(N_{ml}+N_{mg}\right)_{ij,out} - \left(N_{ml}+N_{mg}\right)_{ij,in}\right] + Q_m = V_i \frac{\left(S_l x_m \overline{\rho}_l + S_g y_m \overline{\rho}_g\right)^{t+\Delta t} - \left(S_l x_m \overline{\rho}_l + S_g y_m \overline{\rho}_g\right)^{t}}{\Delta t} \tag{A.4}$$

Molar concentrations of condensate and gas are defined as follows based on molar fractions and molar densities:

$$C_{ml} = x_m \frac{n}{V} = x_m \frac{\frac{m}{MW}}{\frac{m}{\rho_l}} = x_m \frac{\rho_l}{MW} = x_m \overline{\rho}_l \ \left(kmol\,/\,m^3\right) \tag{A.5}$$

$$C_{mg} = y_m \frac{n}{V} = y_m \frac{\frac{m}{MW}}{\frac{m}{\rho_g}} = y_m \frac{\rho_g}{MW} = y_m \overline{\rho}_g \ \left(kmol \,/\, m^3\right) \tag{A.6}$$

$$\overline{\rho}_f = molar\ density\ of\ fluid\ in\ \left(\frac{kmol}{m^3}\right) = \frac{\rho_f}{MW_f} \tag{A.7}$$

$$\rho_f = mass\ density\ of\ fluid\ in\ \left(kg \,/\, m^3\right) \tag{A.8}$$

Next, using molar concentrations, the molar material balance is written as a function of components molar fractions in the liquid and gas phase.

$$-\sum_j^{N_{cap}} \left[\left(C_{ml} v_{ml} A + C_{mg} v_{mg} A\right)_{ij,out} - \left(C_{ml} v_{ml} A + C_{mg} v_{mg} A\right)_{ij,in} \right] + Q_m = V_i \frac{\left(S_l x_m \overline{\rho}_l + S_g y_m \overline{\rho}_g\right)^{t+\Delta t} - \left(S_l x_m \overline{\rho}_l + S_g y_m \overline{\rho}_g\right)^{t}}{\Delta t} \tag{A.9}$$

$$-\sum_j^{N_{cap}} \left[\left(x_m \overline{\rho}_l v_{ml} A + y_m \overline{\rho}_g v_{mg} A\right)_{ij,out} - \left(x_m \overline{\rho}_l v_{ml} A + y_m \overline{\rho}_g v_{mg} A\right)_{ij,in} \right] + Q_m = V_i \frac{\left(S_l x_m \overline{\rho}_l + S_g y_m \overline{\rho}_g\right)^{t+\Delta t} - \left(S_l x_m \overline{\rho}_l + S_g y_m \overline{\rho}_g\right)^{t}}{\Delta t} \tag{A.10}$$

$$-\sum_j^{N_{cap}} \left[\left(x_m \overline{\rho}_l v_{ml} A + y_m \overline{\rho}_g v_{mg} A\right)_{ijout} - \left(x_m \overline{\rho}_l v_{ml} A + y_m \overline{\rho}_g v_{mg} A\right)_{ijin} \right] + Q_m = V_i \frac{\partial}{\partial t} \left(S_l x_m \overline{\rho}_l + S_g y_m \overline{\rho}_g\right) \tag{A.11}$$

The fluid molar velocity in the throat is defined and is given below as a function of the fluid conductance and the fluid potential gradient over length of the throat.

$$V_{mf.ij} A = Q_{mf.ij} = g_{mf.ij} \left(\Phi_{f.i} - \Phi_{f.j}\right) \tag{A.12}$$

$$\Phi_{f,i} = P_{f,i} + \rho_f g D_i \tag{A.13}$$

Applying fluid conductance and the terms for potential gradients, the molar conservation equation is reformed as:

$$-\sum_j^{N_{cap}} \left[\left(x_m \overline{\rho}_l g_l \Delta\Phi_l + y_m \overline{\rho}_g g_g \Delta\Phi_g\right)_{ij,out} - \left(x_m \overline{\rho}_l g_l \Delta\Phi_l + y_m \overline{\rho}_g g_g \Delta\Phi_g\right)_{ij,in} \right] + Q_m = V_i \frac{\partial}{\partial t} \left(S_l x_m \overline{\rho}_l + S_g y_m \overline{\rho}_g\right) \tag{A.14}$$

Assuming a laminar flow for a single-phase flow in the circular capillary, the single-phase conductance, g_p can be derived analytically using Poiseuille's law:

$$g_p = k \frac{A^2 G}{\mu_p} = \frac{1}{2} \frac{A^2 G}{\mu_p} \quad ; p = \text{gas or liquid phase} \tag{A.15}$$

where k value for equilateral triangles and squares are 3/5 and 0.5623 respectively and G is the geometrical shape factor defined:

$$G = \frac{A}{P^2} \tag{A.16}$$

Finally, ignoring the capillary pressure in the pore body nodes with assumption of low-IFT flow in a conventional gas-condensate reservoir leads to the ultimate form of molar conservation equation as Eq. (A.17):

$$-\sum_j^{N_{cap}} C_{ij} H_{ij} \left[\left(x_m \overline{\rho}_l g_l + y_m \overline{\rho}_g g_g\right)_{ij} \right] \Delta\Phi_{g,ij} + Q_m = V_i \frac{\partial}{\partial t} \left(S_l x_m \overline{\rho}_l + S_g y_m \overline{\rho}_g\right), m = 1 \ldots n_c \tag{A.17}$$

where $\Delta\Phi_{ij} = \Delta\Phi_{g,ij} = \Delta\Phi_{l,ij}$. The terms H_{ij} and H^e_{ij} are step functions depending on conditions for corner (film) flow, snap-off and condensate bridge displacement in the corresponding throat.

$\Delta\Phi_{ij}$ is the potential gradient over the throat length given in Eq. (A.18), which is defined based on the phase (gas) pressures in the pore body nodes, i and j linked to the throat, ij. The pressure gradient required to mobilize the condensate bridge in the capillary, ij defined as ΔP^e_{ij} is also included when the condensate bridge is displaced by the increase of gas pressure induced by the viscous force.

$$\Delta\Phi_{ij} = \Delta\Phi_{g,ij} = P_{g,i} - P_{g,j} - H^e_{ij} \Delta P^e_{ij} \tag{A.18}$$

Appendix B. Time step selection

There are only a few studies on gas condensation flow based on the compositional pore-network models, which have presented a procedure for the time step selection due to the complex thermodynamic phase behavior of gas-condensate systems in comparison to multiphase incompressible flow systems. For immiscible incompressible two-phase flow, Joekar Niasar and Personeel (2010) determined the time step based on the required time to fill a pore body by the nonwetting phase or wetting phase depending on the process. The same procedure has also been used by Mogensen et al. (1999), Joekar-Niasar and Hassanizadeh (2012) and Wu et al. (2020).

The selection of the minimum residence time for the time step increases the computational expense of dynamic pore-network models. For modeling dynamic two-phase flow, Chen et al. (2020) proposed an improved scheme for all three methods (fully implicit (FI), implicit pressure explicit saturation (IMPES), and implicit pressure semi-implicit saturation (IMP-SIMS)). A physically constrained time step selection scheme was

implemented; 1) constraint for the wetting phase to be in the range of irreducible residual wetting phase saturation, and 2) for each pore body i, only the largest uninvaded pore throat connected to the pore body is allowed to be invaded within one time step. Thus, the local maximum time step size was determined for all pore bodies and thereby the minimum value of all local time steps for the entire network was used as the global time step size. They stated that the FI approach in comparison to IMPES and IMP-SES methods, is globally mass conservative in pore-network modeling simulation regardless of the type of pore morphology. On the other hand, the wetting phase saturation stays in the physical range because of the iterative nature of the FI method, in which the pressure and saturation are updated simultaneously.

The reported time step for gas-condensate PNM of Jamiolahmady et al. (2003) was based on the evolution time of all pores and they selected the value of evolution time representing the maximum evolution time for the class of pores (containing 0.1% of all pores) that close first) as the time step. Momeni et al. (2017) considered the condensate phase residing in the pore throat corners and calculated closure time in each throat by dividing the number of moles of gas needed to close each throat by the current molar flow rate of gas in each throat. Then, the lowest time duration calculated for closing the throats in the model was chosen as the suitable time step for the whole network.

In our study, the timestep was selected to satisfy the following criteria: the residence time to fill the smallest throat in a control volume, as well as an acceptable courant number range applied in the work of Zhang et al. (2015), and consideration of the concept of pressure diffusion (Muskat, 1937) (i.e., drainage radius; how far pressure diffuses during a transient test). We followed the radius of investigation formulation (Van Poolen, 1964; Kuchuk, 2009), implementing in the pore network flow. A pressure transient test was performed on the pore network, and the time, in which a pressure impulse spreads along the network during a draw-down test was calculated. Consequently, the selected time step was checked to be small enough so that simulations capture the transient conditions (i.e., the process of trapping and mobilization of gas condensates) happening inside the network prior to approaching the eventual steady-state condition, starting from an initial pressure distribution.

Appendix C. Supplementary data

Supplementary data to this article can be found online at https://doi.org/10.1016/j.geoen.2023.211937.

References

Aker, E., Maloy, J., Hansen, A., Batrouni, G.G., 1998. A two-dimensional network simulator for two-phase flow in porous media. Transport Porous Media 32, 163–186.

Al Harrasi, M.A.W.S., 2011. Fluid Flow Properties of Tight Gas-Condensate Reservoirs. University of Leeds. Doctoral dissertation.

Al-Anazi, H.A., Xiao, J., Al-Eidan, A.A., Buhidma, I.M., Ahmed, M.S., Al-Faifi, M., Assiri, W.J., 2007. Gas productivity enhancement by wettability alteration of gas-condensate reservoirs. In: European Formation Damage Conference. OnePetro.

Al-Gharbi, M.S., Blunt, M.J., 2005. Dynamic network modeling of two-phase drainage in porous media. Phys. Rev. E 71, 016308.

Al-Harrasi, M., Grattoni, C., Fisher, Q., Lane, M., 2013. Gas condensate flow behaviour within tight reservoirs. In: SPE Unconventional Gas Conference and Exhibition. Society of Petroleum Engineers.

Al-Kharusi, B.S., 2000. Modelling of gas condensate relative permeability and its impact on prediction of reservoir performance. SPE Reservoir Eng. 871–880.

Asar, H., Handy, L.L., 1988. Influence of interfacial tension on gas/oil relative permeability in a gas-condensate system. SPE Reservoir Eng. 3 (1), 257–264.

Bardon, C., Longeron, D.G., 1980. Influence of very low interfacial tensions on relative permeability. Soc. Petrol. Eng. J. 20 (5), 391–401.

Beresnev, I.A., Li, W., Vigil, R.D., 2009. Condition for break-up of non-wetting fluids in sinusoidally constricted capillary channels. Transport Porous Media 80 (3), 581.

Blom, S.M.P., Hagoort, J., Soetekouw, D.P.N., 2000. Relative permeability at near-critical conditions. SPE J. 5 (2), 172–181.

Blunt, M., Jackson, M.D., Piri, M., Valvatne, P.H., 2002. Detailed physics, predictive capabilities and macroscopic consequences for pore-network models of multiphase flow. Adv. Water Resour. 25, 1069–1089.

Blunt, M.J., 1997. Effects of heterogeneity and wetting on relative permeability using pore level modeling. SPE J. 2 (1), 70–87.

Bustos, C.I., Toledo, P.G., 2004. Pore shape effects on the relative permeability of gas and condensate in three-dimensional pore networks. Transport Porous Media 55 (2), 247–251.

Bustos, C.I., Toledo, P.G., 2003. Pore-level modeling of gas and condensate flow in two- and three-dimensional pore networks: pore size distribution effects on the relative permeability of gas and condensate. Transport Porous Media 53 (3), 281–315.

Cai, J.C., Chen, Y., Qiao, J.C., Yang, L., Zeng, J.H., Sun, C.H., 2022. Determination of dynamic capillary effect on two-phase flow in porous media: a perspective from various methods. Petrol. Sci. 19 (4), 1641–1652.

Chen, S., Jiang, J., Guo, B., 2021. A pore-network-based upscaling framework for the nanoconfined phase behavior in shale rocks. Chem. Eng. J. 417, 129210.

Chen, S., Qin, C., Guo, B., 2020. Fully implicit dynamic pore-network modeling of two-phase flow and phase change in porous media. Water Resour. Res. 56, e2020WR028510.

Class, H., Helmig, R., Bastian, P., 2002. Numerical simulation of non-isothermal multiphase multicomponent processes in porousmedia: 1. An efficient solution technique. Adv. Water Resour. 25 (5), 533–550.

Coskuner, G., 1997. Microvisual study of multiphase gas condensate flow in porous media. Transport Porous Media 28 (1), 1–18.

Cui, R., Hassanizadeh, S.M., Sun, S., 2022. Pore-network modeling of flow in shale nanopores: network structure, flow principles, and computational algorithms. Earth Sci. Rev., 104203

Danesh, A., 1998. PVT and Phase Behaviour of Petroleum Reservoir Fluids. Elsevier.

Danesh, A., Khazam, M., Henderson, G., Tehrani, D., Peden, J., 1994. Gas condensate recovery studies. In: DTI Improved Oil Recovery and Research Dissemination Seminar, (London).

Danesh, A., Krinis, D., Henderson, G.D., Peden, J.M., 1990. Visual investigation of retrograde phenomena and gas condensate flow in porous media. Rev. Inst. Fr. Petrol 45 (1), 79–87.

Daneshian, B., Habibagahi, G., Nikooee, E., 2021. Determination of unsaturated hydraulic conductivity of sandy soils: a new pore network approach. Acta Geotechnica 16 (2), 449–466.

Dong, H., Blunt, M.J., 2009. Pore-network extraction from micro-computerized-tomography images. Phys. Rev. E 80, 036307.

Dong, H., 2008. Micro-CT Imaging and Pore Network Extraction. Ph.D. thesis. Department of Earth Science and Engineering, Imperial College London.

Fahimpour, J., Jamiolahmady, M., 2015. An improved understanding of performance of wettability alteration for condensate banking removal under steady-state flow conditions. In: Abu Dhabi International Petroleum Exhibition and Conference. Society of Petroleum Engineers.

Fang, F., Firoozabadi, A., Abbaszadeh, M., Radke, C., 1996. A phenomenological modeling of critical condensate saturation. In: SPE Annual Technical Conference and Exhibition. Society of Petroleum Engineers.

Fathi, H., Raoof, A., Mansouri, S.H., 2017. Insights into the role of wettability in cathode catalyst layer of proton exchange membrane fuel cell; pore scale immiscible flow and transport processes. Journal of Power Sources 349, 57–67.

Fatt, I., 1956. The network model of porous media. Trans. AIME 207 (01), 144–181.

Firincioglu, T., Blunt, M.J., Zhou, D., 1999. Three-phase flow and wettability effects in triangular capillaries. Colloids Surf. A Physicochem. Eng. Asp. 155 (2–3), 259–276.

Gholampour, F., Mahdiyar, H., 2019. A new correlation for relative permeability in gas-condensate reservoirs. J. Petrol. Sci. Eng. 172, 831–838.

Golparvar, A., Zhou, Y., Wu, K., Ma, J., Yu, Z., 2018. A comprehensive review of pore-scale modeling methodologies for multiphase flow in porous media. Advances in Geo-Energy Research 2 (4), 418–440.

Haniff, M.S., Ali, J.K., 1990. Relative permeability and low tension fluid flow in gas condensate systems. In: European Petroleum Conference. OnePetro.

He, M., Zhou, Y., Wu, K., Hu, Y., Feng, D., Zhang, T., Liu, Q., Li, X., 2021. Pore network modeling of thin water film and its influence on relative permeability curves in tight formations. Fuel 289, 119828.

Henderson, G.D., Danesh, A., Tehrani, D.H., Peden, J.M., 1997. The effect of velocity and interfacial tension on the relative permeability of gas condensate fluids in the wellbore region. J. Petrol. Sci. Eng. 17, 265–273.

Henderson, G.D., Danesh, A., Tehrani, D.H., 2001. Effect of positive rate sensitivity and inertia on gas condensate permeability at high velocity. Petrol. Geosci. 7 (1), 45–50.

Henderson, G.D., Danesh, A., Tehrani, D.H., Al-Shaidi, S., Peden, J.M., 1998. Measurement and correlation of gas condensate relative permeability by the steady-state method. SPE Reservoir Eval. Eng. 1 (2), 134–140.

Henderson, G.D., Danesh, A., Tehrani, D.H., Al-Shaidi, S., Peden, J.M., 1996. Measurement and correlation of gas condensate relative permeability by the steady-state method. SPE J. 1 (2), 191–202.

Henderson, G.D., Danesh, A., Tehrani, D.H., Peden, J.M., 1995. The effect of velocity and interfacial tension on the relative permeability of gas condensate fluids in the wellbore region. In: IOR 8th European Symposium on Improved Oil Recovery.

Hoseinpour, S.A., Madhi, M., Norouzi, H., Soulgani, B.S., Mohammadi, A.H., 2019. Condensate blockage alleviation around gas-condensate producing wells using wettability alteration. J. Nat. Gas Sci. Eng. 62, 214–223.

Hosseinkhani, E., Habibagahi, G., Nikooee, E., 2023. Cyclic modeling of unsaturated sands using a pore-scale hydromechanical approach. Int. J. Numer. Anal. Methods GeoMech. 47 (3), 457–481.
Hosseinzadegan, A., Raoof, A., Mahdiyar, H., Nikooee, E., Ghaedi, M., Qajar, J., 2023. Review on pore-network modeling studies of gas-condensate flow: pore structure, mechanisms, and implementations. Geoenergy Sci. Eng., 211693
Hughes, R.G., Blunt, M.J., 2000. Pore scale modeling of rate effects in imbibition. Transport Porous Media 40 (3), 295–322.
Hui, M.H., Blunt, M.J., 2000. Effects of wettability on three-phase flow in porous media. J. Phys. Chem. B 104 (16), 3833–3845.
Jamiolahmady, M., Danesh, A., Tehrani, D.H., Duncan, D.B., 2000. A mechanistic model of gas-condensate flow in pores. Transport Porous Media 41 (1), 17–46.
Jamiolahmady, M., Danesh, A., Tehrani, D.H., Duncan, D.B., 2003. Positive effect of flow velocity on gas–condensate relative permeability: network modelling and comparison with experimental results. Transport Porous Media 52, 159–183.
Joekar-Niasar, V., Personeel, S.A., 2010. The Immiscibles: Capillarity Effects in Porous Media-Pore-Network Modelling. Geologica Ultraiectina (318) (Doctoral dissertation, University Utrecht).
Joekar-Niasar, V., Hassanizadeh, S., 2012. Analysis of fundamentals of two-phase flow in porous media using dynamic pore-network models: a review. Crit. Rev. Environ. Sci. Technol. 42 (18), 1895–1976.
Karandish, G.R., Rahimpour, M.R., Sharifzadeh, S., Dadkhah, A.A., 2015. Wettability alteration in gas-condensate carbonate reservoir using anionic fluorinated treatment. Chem. Eng. Res. Des. 93, 554–564.
Khaksar, H., Habibagahi, G., Nikooee, E., 2013. SWRC modeling in unsaturated soils: a pore network approach. In: Poromechanics V: Proceedings of the Fifth Biot Conference on Poromechanics, pp. 1570–1579.
Khaksar, H., Nikooee, E., Habibagahi, G., Majid Hassanizadeh, S., 2015. Modeling Temperature Effects on Soil Water Retention Curve: a Pore Network Approach.
Knudsen, H.A., Hansen, A., 2002. Relation between pressure and fractional flow in two-phase flow in porous media. Phys. Rev. 65, 1–10.
Koplik, J., Lasseter, T.J., 1985. Two-phase flow in random network models of porous media. Soc. Petrol. Eng. J. 25 (1), 89–100.
Kuchuk, F.J., 2009. Radius of investigation for reserve estimation from pressure transient well tests. In: SPE Middle East Oil and Gas Show and Conference. OnePetro.
Labed, I., Oyeneyin, B., Oluyemi, G., 2018. Gas-condensate flow modelling for shale reservoirs. J. Nat. Gas Sci. Eng. 59, 156–167.
Lauser, A., 2014. Theory and Numerical Applications of Compositional Multi-phase Flow in Porous Media (Dissertation). Mitteilungen/Institut für Wasser- und Umweltsystemmodellierung, Universität Stuttgart, p. 228.
Lauser, A., Hager, C., Helmig, R., Wohlmuth, B., 2011. A new approach for phase transitions in miscible multi-phase flow in porous media. Adv. Water Resour. 34 (8), 957–966.
Li, K., Firoozabadi, A., 2000. Phenomenological modeling of critical condensate saturation and relative permeabilities in gas/condensate systems. SPE J. 5 (2), 138–147.
Li, K., Liu, Y., Zheng, H., Huang, G., Li, G., 2011. Enhanced gas-condensate production by wettability alteration to gas wetness. J. Petrol. Sci. Eng. 78 (2), 505–509.
Li, M., Qu, J., Ocłoń, P., Wei, J., Tao, W., 2020. 3D numerical simulation of condensation and condensate behaviors on textured structures using lattice Boltzmann method. Int. J. Heat Mass Tran. 160, 120198.
Liu, Y., Zheng, H., Huang, G., Li, G., Li, K., 2006. Improving production in gas/condensate reservoirs by wettability alteration to gas wetness. In: SPE/DOE Symposium on Improved Oil Recovery. OnePetro.
Lohrenz, J., Bray, B.G., Clark, C.R., 1964. Calculating viscosities of reservoir fluids from their compositions. J. Petrol. Technol. 16, 1–171.
Lovoll, G., Méheust, Y., Maloy, K.J., Aker, E., Schmittbuhl, J., 2005. Competition of gravity, capillary and viscous forces during drainage in a two-dimensional porous medium, a pore scale study. Energy 30, 861–872.
Mahdiyar, H., Jamiolahmady, M., 2014. Optimization of hydraulic fracture geometry in gas condensate reservoirs. Fuel 119, 27–37.
Mason, G., Morrow, N.R., 1991. Capillary behavior of a perfectly wetting liquid in irregular triangular tubes. J. Colloid Interface Sci. 141 (1), 262–274.
Mehmani, A., Verma, R., Prodanović, M., 2020. Pore-scale modeling of carbonates. Marine and Petroleum Geology 114, 104141.
Michelsen, M.L., 1982. The isothermal flash problem. Part I. Stability. Fluid Phase Equil. 9, 1–19.
Mogensen, K., Stenby, E., Banerjee, S., Barker, V.A., 1999. Comparison of iterative methods for computing the pressure field in a dynamic network model. Transport Porous Media 37, 277–301.
Mohammadi, S., Sorbie, K., Danesh, A., Peden, J., 1990. Pore-level modelling of gas-condensate flow through horizontal porous media. In: SPE Annual Technical Conference and Exhibition. Society of Petroleum Engineers.
Momeni, A., Dadvar, M., Hekmatzadeh, M., Dabir, B., 2017. 3D pore network modeling and simulation for dynamic displacement of gas and condensate in wellbore region. Int. J. Multiphas. Flow 97, 147–156.
Mott, R., Cable, A., Spearing, M., 2000. Measurements and Simulation of Inertial and High Capillary Number Flow Phenomena in Gas-Condensate Relative Permeability. SPE 62932. AEA Technology.
Munkerud, P.K., Torsaeter, O., 1995. The effects of interfacial tension and spreading on relative permeability in gas condensate systems. In: IOR 1995-8th European Symposium on Improved Oil Recovery (Pp. Cp-107). European Association of Geoscientists & Engineers.
Muskat, M., 1937. The flow of fluids through porous media. J. Appl. Phys. 8 (4), 274–282.
Nikooee, E., Habibagahi, G., Khaksar, H., Hassanizadeh, S., Raoof, A., 2014. Pore network modeling of unsaturated soils: fundamentals, recent advancements and future perspectives. In: Numerical Methods in Geotechnical Engineering-NUMGE, 2014, pp. 1007–1012.
Nikooee, E., Sweijen, T., Hassanizadeh, S.M., 2016. Determination of the relationship among capillary pressure, saturation and interfacial area: a pore unit assembly approach. In: E3S Web of Conferences (vol. 9, p. 02002). EDP Sciences.
Noh, M., Firoozabadi, A., 2008. Wettability alteration in gas-condensate reservoirs to mitigate well deliverability loss by water blocking. SPE Reservoir Eval. Eng. 11 (4), 676–685.
Oren, P.E., Bakke, S., Arntzen, O.J., 1998. Extending predictive capabilities to network models. SPE J. 3 (4), 324–336.
Panja, P., Velasco, R., Deo, M., 2020. Understanding and modeling of gas-condensate flow in porous media. Adv. Geo-Energy Res. 4 (2), 173.
Patzek, T.W., Silin, D.B., 2001. Shape factor and hydraulic conductance in noncircular capillaries: I. One-phase creeping flow. J. Colloid Interface Sci. 236 (2), 295–304.
Peng, D.-Y., Robinson, D.B., 1976. A new two-constant equation of state. Ind. Eng. Chem. Fundam. 15 (1), 59–64.
Piri, M., Blunt, M.J., 2005. Three-dimensional mixed-wet random pore-scale network modeling of two-and three-phase flow in porous media. I. Model description. Phys. Rev. 71 (2), 026301.
Raeini, A.Q., Bijeljic, B., Blunt, 2015. Modelling capillary trapping using finite-volume simulation of two-phase flow directly on micro-CT images. Advances in Water Resources 83, 102–110.
Raoof, A., Hassanizadeh, S.M., 2010. A new method for generating pore-network models of porous media. Transport Porous Media 81 (3), 391–407.
Raoof, A., Hassanizadeh, S.M., 2012. A new formulation for pore-network modeling of two-phase flow. Water Resour. Res. 48, W01514.
Raoof, A., Nick, H.M., Hassanizadeh, S.M., Spiers, C.J., 2013. PoreFlow: a complex pore-network model for simulation of reactive transport in variably saturated porous media. Comput. Geosci. 61, 160–174.
Reis, P.K., Carvalho, M.S., 2020. Pore-scale analysis of condensate blockage mitigation by wettability alteration. Energies 13 (18), 4673.
Reis, P.K., Carvalho, M.S., 2021. Pore-scale compositional modeling of gas-condensate flow: effects of interfacial tension and flow velocity on relative permeability. J. Petrol. Sci. Eng. 202, 108454.
Reis, P.K., Carvalho, M.S., 2022. Pore-scale analysis of gas injection in gas-condensate reservoirs. J. Petrol. Sci. Eng. 212, 110189.
Rostami, A., Habibagahi, G., Ajdari, M., Nikooee, E., 2015. Pore network investigation on hysteresis phenomena and influence of stress state on the SWRC. Int. J. GeoMech. 15 (5), 04014072.
Santos, M., Carvalho, M., 2020. Pore network model for retrograde gas flow in porous media. J. Petrol. Sci. Eng. 185, 106635.
Song, W., Liu, L., Wang, D., Li, Y., Prodanović, M., Yao, J., 2020. Nanoscale confined multicomponent hydrocarbon thermodynamic phase behavior and multiphase transport ability in nanoporous material. Chem. Eng. J. 382, 122974.
Sweijen, T., Aslannejad, H., Hassanizadeh, S.M., 2017. Capillary pressure–saturation relationships for porous granular materials: pore morphology method vs. pore unit assembly method. Adv. Water Resour. 107, 22–31.
Sweijen, T., Nikooee, E., Hassanizadeh, S.M., Chareyre, B., 2016. The effects of swelling and porosity change on capillarity: DEM coupled with a pore-unit assembly method. Transport Porous Media 113 (1), 207–226.
Thompson, K.E., 2002. Pore-scale modeling of fluid transport in disordered fibrous materials. AIChE J. 48 (7), 1369–1389.
Valvatne, P.H., Blunt, M.J., 2004. Predictive pore-scale modeling of two-phase flow in mixed wet media. Water Resour. Res. 40 (7).
Van Poolen, H.K., 1964. Radius-of-drainage and stabilization-time equations. Oil Gas J. 62, 138–146.
Wang, X., Mohanty, K., 1999. Critical condensate saturation in porous media. J. Colloid Interface Sci. 214 (2), 416–426.
Wang, X., Mohanty, K.K., 2000. Pore-network model of flow in gas/condensate reservoirs. SPE J. 5 (4), 426–434.
Weishaupt, K., Helmig, R., 2021. A dynamic and fully implicit non-isothermal, two-phase, two-component pore-network model coupled to single-phase free flow for the pore-scale description of evaporation processes. Water Resour. Res. 57 (4), e2020WR028772.
Wu, R., Zhang, T., Ye, C., Zhao, C.Y., Tsotsas, E., Kharaghani, A., 2020. Pore network model of evaporation in porous media with continuous and discontinuous corner films. Phys. Rev. Fluids 5 (1), 014307.
Xiong, Q., Baychev, T.G., Jivkov, A.P., 2016. Review of pore network modelling of porous media: experimental characterisations, network constructions and applications to reactive transport. J. Contam. Hydrol. 192, 101–117.
Yi, Z., Lin, M., Jiang, W., Zhang, Z., Li, H., Gao, J., 2017. Pore network extraction from pore space images of various porous media systems. Water Resour. Res. 53, 3424–3445.
Younes, N., Benseghier, Z., Millet, O., Wautier, A., Nicot, F., Wan, R., 2022. Phase-field Lattice Boltzmann model for liquid bridges and coalescence in wet granular media. Powder Technol. 411, 117942.
Yu, H., Chen, J., Zhu, Y., Wang, F., Wu, H., 2017. Multiscale transport mechanism of shale gas in micro/nano-pores. Int. J. Heat Mass Tran. 111, 1172–1180.
Yu, H., Fan, J., Chen, J., Zhu, Y., Wu, H., 2018. Pressure-dependent transport characteristic of methane gas in slit nanopores. Int. J. Heat Mass Tran. 123, 657–667.
Yu, H., Fan, J., Xia, J., Liu, H., Wu, H., 2020. Multiscale gas transport behavior in heterogeneous shale matrix consisting of organic and inorganic nanopores. J. Nat. Gas Sci. Eng. 75, 103139.

Yu, H., Xu, H., Fan, J., Zhu, Y.B., Wang, F., Wu, H., 2021. Transport of shale gas in microporous/nanoporous media: molecular to pore-scale simulations. Energy Fuel. 35 (2), 911–943.
Yu, H., Zhu, Y., Jin, X., Liu, H., Wu, H., 2019. Multiscale simulations of shale gas transport in micro/nano-porous shale matrix considering pore structure influence. J. Nat. Gas Sci. Eng. 64, 28–40.
Zhang, P., Hu, L., Meegoda, J.N., Gao, S., 2015. Micro/nano-pore network analysis of gas flow in shale matrix. Sci. Rep. 5 (1), 13501.
Zhang, S., Jiang, G.C., Wang, L., Qing, W., Guo, H.T., Tang, X.G., Bai, D.G., 2014. Wettability alteration to intermediate gas-wetting in low-permeability gas-condensate reservoirs. J. Pet. Explor. Prod. Technol. 4 (3), 301–308.
Zhao, B., MacMinn, C.W., Primkulov, B.K., Chen, Y., Valocchi, A.J., Zhao, J., Kang, Q., Bruning, K., McClure, J.E., Miller, C.T., Fakhari, A., 2019. Comprehensive comparison of pore-scale models for multiphase flow in porous media. Proceedings of the National Academy of Sciences 116 (28), 13799–13806.
Zhou, D., Blunt, M.J., Orr, F.M., 1997. Hydrocarbon drainage along corners of noncircular capillaries. J. Colloid Interface Sci. 187 (1), 11–21.